

## FULLY DECOUPLED ENERGY-STABLE NUMERICAL SCHEMES FOR TWO-PHASE COUPLED POROUS MEDIA AND FREE FLOW WITH DIFFERENT DENSITIES AND VISCOSITIES

YALI GAO<sup>1</sup>, XIAOMING HE<sup>2,\*</sup>, TAO LIN<sup>3</sup> AND YANPING LIN<sup>4</sup>

**Abstract.** In this article, we consider a phase field model with different densities and viscosities for the coupled two-phase porous media flow and two-phase free flow, as well as the corresponding numerical simulation. This model consists of three parts: a Cahn–Hilliard–Darcy system with different densities/viscosities describing the porous media flow in matrix, a Cahn–Hilliard–Navier–Stokes system with different densities/viscosities describing the free fluid in conduit, and seven interface conditions coupling the flows in the matrix and the conduit. Based on the separate Cahn–Hilliard equations in the porous media region and the free flow region, a weak formulation is proposed to incorporate the two-phase systems of the two regions and the seven interface conditions between them, and the corresponding energy law is proved for the model. A fully decoupled numerical scheme, including the novel decoupling of the Cahn–Hilliard equations through the four phase interface conditions, is developed to solve this coupled nonlinear phase field model. An energy-law preservation is analyzed for the temporal semi-discretization scheme. Furthermore, a fully discretized Galerkin finite element method is proposed. Six numerical examples are provided to demonstrate the accuracy, discrete energy law, and applicability of the proposed fully decoupled scheme.

**Mathematics Subject Classification.** 65M12, 35Q35, 65M15, 65M60, 76D05.

Received May 28, 2022. Accepted February 2, 2023.

### 1. INTRODUCTION

Multi-phase flow appears in a wide range of applications, from fluid dynamics and fluid-surfactant dynamics to solid physics and biomedical sciences. Multi-phase flow in karstic geometry, as a typical multi-phase flow in coupled free flow region and porous medium region, plays a crucial role in the research of contaminant transport in groundwater system [59, 68, 83, 86]. Related work can be extended to study other important problems with this type of coupled flows, such as oil recovery in petroleum engineering [42, 88, 96], cardiovascular blood flow

---

*Keywords and phrases.* Cahn–Hilliard–Navier–Stokes–Darcy model, phase-field model, karstic geometry, different densities, fully decoupled, energy stability.

<sup>1</sup> Department of Mathematics and Statistics, Northwestern Polytechnical University, Xi'an Shaanxi 710129, P.R. China.

<sup>2</sup> Department of Mathematics and Statistics, Missouri University of Science and Technology, Rolla, MO 65409, USA.

<sup>3</sup> Department of Mathematics, Virginia Tech, Blacksburg, VA 24061, USA.

<sup>4</sup> Department of Applied Mathematics, The Hong Kong Polytechnic University, Hung Hom, Hong Kong.

\*Corresponding author: [hex@mst.edu](mailto:hex@mst.edu)

[37], and proton exchange membrane fuel cell [84]. Therefore, it is worthwhile to develop efficient numerical schemes for studying these coupled multi-phase flow problems.

In the past two decades, scientists have published research results about single-phase models of the coupled free flow and porous media flow [7, 17, 21, 28, 53, 60, 77], which are composed of Stokes/Navier–Stokes equation, Darcy’s law, and three interface conditions coupling these two parts. There have been abundant numerical attempts for these models, for instance, domain decomposition methods [10, 18, 19, 25, 31, 33, 48], discontinuous Galerkin method [41, 54, 65, 76], two-grid/multi-grid methods [3, 14, 70], and many others. However, there have been much less works about the important multi-phase models of the coupled free flow and porous media flow which are much more challenging than the single phase models in this area.

Phase-field has become a popular modeling technique in simulating multi-phase flow [11, 12, 64, 66, 67, 73, 89, 95] as a viable tool to describe the interfacial motion between two immiscible fluids. By this technique, the interface is described by a smooth layer with finite width so that the singularities across the interface is removed [34, 56, 80]. One of its attractive features is that it automatically captures the interface transition in numerical simulation based on the energy law [57, 62].

In recent years, the phase field modeling for two-phase flow across the interface between free flow region and porous medium region has started to attract researchers’ attention [5, 26, 27, 30, 39, 49, 50, 82]. Among the models proposed in these works, we will consider the modeling ideas in [27, 39, 49, 50]. Han *et al.* [49] deduced a family of phase field models for the two-phase flows in karstic geometry based on a fundamental diffuse interface model with constant density/viscosity, which preserves some physical property, *e.g.*, energy law. Then, for these models, Chen *et al.* [27] and Han *et al.* [50] systematically studied the existence and uniqueness of the weak solution, and proposed and analyzed some unconditionally stable numerical algorithms for the involved Cahn–Hilliard–Stokes–Darcy system with constant density/viscosity. Gao *et al.* [39] developed a partially decoupled numerical method for the Cahn–Hilliard–Navier–Stokes–Darcy (CHNSD) system with constant density/viscosity. Gao *et al.* [40] developed another type of partially decoupled numerical method in a simplified framework for CHNSD model with different densities/viscosities based on the idea of a single Cahn–Hilliard equation on the whole domain (including both the porous media region and the free flow region). Hence it does not consider the four phase field interface conditions but only the three flow field interface conditions in the design of the partially decoupling scheme. Due to the large scale computation of the realistic applications of the CHNSD system with different densities/viscosities, a fully decoupled scheme is in great needs to further improve the computational efficiency. Therefore, in this article, we will develop a fully decoupled scheme, including the decoupling of the Cahn–Hilliard equations in the porous media region and the free flow region through the four phase field interface conditions, the decoupling of the flow fields through the three flow interface conditions, the decoupling between the phase field and flow field by operator splitting, the decoupling between the velocity and pressure by rotational pressure projection, and the invariant energy quadratization (IEQ) method to handle the nonlinear potential term.

The CHNSD model with different density/viscosity considered in this article consists of a coupled Cahn–Hilliard–Navier–Stokes system with different density/viscosity describing the dynamics of free flow fluid in conduit, a coupled Cahn–Hilliard–Darcy (or Cahn–Hilliard–Hele–Shaw) system with different density/viscosity describing the evolution of porous media flow in matrix, and seven interface conditions describing the transition of two-phase flow across the interface between the conduit region and the matrix region. Three interface conditions are for the flow field and the other four interface conditions are for the phase field. For this sophisticated CHNSD model with different densities and viscosities, here are a few major numerical challenges: (i) the coupling of free flow region and porous media region demands high computing costs; (ii) different densities and viscosity cause the strong coupling and large derivative across the interface between two fluids; (iii) the relative slow motion in matrix requires long time numerical simulation; (iv) the coupling between the phase function and the flow (in both regions) mandates complicated computation; (v) the inherent stiffness in the phase field model associated with the thin transition layer calls for a carefully treatment to capture the evolution of interface between binary immiscible fluids. Even though methods dealing with one of the challenges mentioned above may exist, a straightforward combination of the existing methods cannot address these challenges posed by

such a complicated coupled system. It is our intention to develop efficient and stable numerical schemes for simulating this CHNSD model with different density/viscosity.

Techniques can be found in the literature for efficiently dealing with the stiffness in diffuse interface models, for example, the convex splitting method [6, 43, 44, 94], the stabilized semi-implicit approach [15, 35, 90], the invariant energy quadratization (IEQ) method [24, 58, 72, 91, 93, 97, 98], the scalar auxiliary variable (SAV) approach [74, 81, 92, 99], the exponential time differencing method [63, 87], etc. The idea of the IEQ is inspired by a Lagrange multiplier method [47]. An essential effect of the IEQ method is to semi-implicitly treat the nonlinear term for phase field type models by making free energy quadratic, which yields a linear system at each time step. The IEQ method requires the nonlinear potential to be bounded from below; nevertheless, most nonlinear potentials usually satisfy this constraints.

In this article, we develop energy-law preserving time-stepping schemes for solving the CHNSD system with different density/viscosity, by using the following ideas. To decouple the computation for fluid equations in free flow region and in porous media region, we adopt a novel weak formulation that weakly enforces interface conditions imposed at the boundary between these two regions. The ideas of the IEQ approach and operator splitting technique will be employed to derive a partially decoupled method. The pressure correction method and stabilization strategy are exploited to design a completely decoupled energy-stable numerical scheme. Following these ideas, a fully decoupled numerical method is developed by cooperating the grad-div technique. The proposed methods solve the two Cahn–Hilliard systems in their own subdomains, respectively, instead of directly solving one Cahn–Hilliard equation on the whole domain [27, 40]. The unconditional stability is proved for the semi-discretization schemes of the two decoupled schemes. It's worth to be pointed out that the decoupling technique for fluid and phase field variables is not trivial because of the different densities considered in the momentum equation for binary fluids. To the best of our knowledge, this is the first work to develop the fully decoupled numerical method for CHNSD system with different densities and viscosities.

The rest of the article is as follows. In Section 2, we present a Cahn–Hilliard–Navier–Stokes–Darcy (CHNSD) model for two-phase flows associated with different densities and viscosities in free fluid region together with porous media. We also prove the energy law of this model. In Section 3, we develop two unconditionally stable decoupled numerical methods by weakly enforcing the domain interface boundary conditions, and discuss their energy dissipation law. In Section 4, we present a fully discrete Galerkin finite element method for this CHNSD model. In Section 5, we present several tests to demonstrate the accuracy and energy law of numerical simulations generated by the proposed schemes, and distinctive features of two-phase flows in the free flow region and the porous media region.

## 2. CAHN–HILLIARD–NAVIER–STOKES–DARCY MODEL

In this section, we briefly present the Cahn–Hilliard–Navier–Stokes–Darcy (CHNSD) model with different densities and viscosities based on the existing Cahn–Hilliard–Stokes–Darcy model [49, 50] and CHNSD model [39] for matched density in karstic geometry. After deriving a weak formulation in cooperate with the interface conditions for this coupled model, we show that the model obeys a dissipative energy law at the PDE level.

### 2.1. Model system

Consider the temporal domain  $[0, T]$  ( $T > 0$ ). Let  $\Omega = \Omega_c \cup \Omega_m \subset \mathbb{R}^d$ , ( $d = 2, 3$ ) be a bounded domain, where  $\Omega_c$  is the free flow region and  $\Omega_m$  is the porous media region. These two subdomains have Lipschitz continuous boundaries  $\partial\Omega_c$  and  $\partial\Omega_m$ , respectively, which form the interface  $\Gamma := \partial\Omega_m \cap \partial\Omega_c$ . Denote the unit normal vector from porous media  $\Omega_m$  to free fluid region  $\Omega_c$  by  $\mathbf{n}_c$  and its opposite vectors by  $\mathbf{n}_m$ . A geometry in two dimensions is depicted in Figure 1.

We consider the double well potential for the Helmholtz free energy  $F(\phi) = \frac{1}{4\epsilon}(\phi^2 - 1)^2$ , and let  $f(\phi) = F'(\phi)$ , where  $\epsilon$  is the thickness of transition layer between two immiscible fluids. Let  $\phi_j$  denote the phase function with respect to  $\Omega_j$  ( $j = c, m$ ) taking distinct values  $\pm 1$  to indicate two different fluid phases and varying smoothly across the diffuse interfacial region. The mobility variable is represented by  $M_j$  ( $j = c, m$ ) as a function of order

parameter  $\phi$ . Variable  $w_j$  ( $j = c, m$ ) is the chemical potential related to phase variable  $\phi_j$ . The parameter  $\gamma$  is the elastic relaxation time of mixing interface.

In this paper, we consider the two-phase fluids with different densities  $\rho$  and viscosities  $\nu$  between fluids as follows

$$\rho = \frac{\rho_1 - \rho_2}{2}\phi + \frac{\rho_1 + \rho_2}{2}, \quad \nu = \frac{\nu_1 - \nu_2}{2}\phi + \frac{\nu_1 + \nu_2}{2}. \quad (2.1)$$

We denote the external gravitational forces by  $\rho \mathbf{g}$  arising from density difference corresponding to the gravity vector  $\mathbf{g} = g\mathbf{j}$ , where the constant  $g$  represents the gravity acceleration and  $\mathbf{j}$  describes the unit vector directing upward.

We assume that the two-phase flow in the porous media region  $\Omega_m$  is described by the Cahn–Hilliard–Darcy (CHD) system as follows:

$$\mathbb{K}^{-1}\mathbf{u}_m + \nabla p_m - w_m \nabla \phi_m = \rho \mathbf{g}, \quad (2.2)$$

$$\nabla \cdot \mathbf{u}_m = 0, \quad (2.3)$$

$$\frac{\partial \phi_m}{\partial t} + \mathbf{u}_m \cdot \nabla \phi_m - \nabla \cdot (M_m \nabla w_m) = 0, \quad (2.4)$$

$$w_m + \gamma \epsilon \Delta \phi_m - \gamma f(\phi_m) = 0, \quad (2.5)$$

where  $t \in [0, T]$ ,  $\mathbf{u}_m$  denotes the advective velocity,  $p_m$  denotes the hydraulic head. The parameter  $\mathbb{K}$  represents hydraulic conductivity tensor. It is noticeable that, by plugging (2.2) into (2.3), one can eliminate the velocity variable  $\mathbf{u}_m$ , and obtain the following Poisson formulation

$$-\nabla \cdot (\mathbb{K} \nabla p_m - \mathbb{K} w_m \nabla \phi_m) = 0. \quad (2.6)$$

We assume that the two-phase flow with different densities and viscosities in the free fluid region  $\Omega_c$  is described by the Cahn–Hilliard–Navier–Stokes (CHNS) system as follows:

$$\rho \left( \frac{\partial \mathbf{u}_c}{\partial t} + (\mathbf{u}_c \cdot \nabla) \mathbf{u}_c \right) - \nabla \cdot \mathbb{T}(\mathbf{u}_c, p_c) - w_c \nabla \phi_c = \rho \mathbf{g}, \quad (2.7)$$

$$\nabla \cdot \mathbf{u}_c = 0, \quad (2.8)$$

$$\frac{\partial \phi_c}{\partial t} + \mathbf{u}_c \cdot \nabla \phi_c - \nabla \cdot (M_c \nabla w_c) = 0, \quad (2.9)$$

$$w_c + \gamma \epsilon \Delta \phi_c - \gamma f(\phi_c) = 0, \quad (2.10)$$

where  $t \in [0, T]$ ,  $\mathbf{u}_c$  and  $p_c$  represent the fluid velocity and the pressure in conduit, respectively.  $\mathbb{T}(\mathbf{u}_c, p_c) = 2\nu \mathbb{D}(\mathbf{u}_c) - p_c \mathbb{I}$  prescribes the stress tensor with the deformation tensor  $\mathbb{D}(\mathbf{u}_c) = (\nabla \mathbf{u}_c + \nabla^T \mathbf{u}_c)/2$  and the identity matrix  $\mathbb{I}$ .

In order to accomplish the exchange of fluids across interface  $\Gamma$  between the conduit and the matrix, we consider the following interface conditions:

$$\phi_c = \phi_m, \quad (2.11)$$

$$w_c = w_m, \quad (2.12)$$

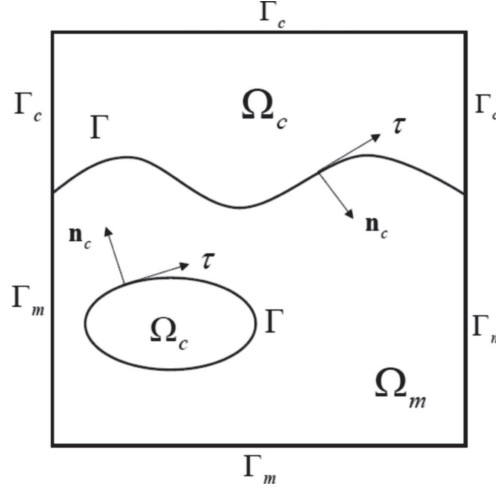
$$\nabla \phi_c \cdot \mathbf{n}_c = -\nabla \phi_m \cdot \mathbf{n}_m, \quad (2.13)$$

$$M_c \nabla w_c \cdot \mathbf{n}_c = -M_m \nabla w_m \cdot \mathbf{n}_m, \quad (2.14)$$

$$\mathbf{u}_c \cdot \mathbf{n}_c = -\mathbf{u}_m \cdot \mathbf{n}_m, \quad (2.15)$$

$$-\mathbf{n}_c \cdot (\mathbb{T}(\mathbf{u}_c, p_c) \cdot \mathbf{n}_c) + \frac{\rho}{2} |\mathbf{u}_c|^2 = p_m, \quad (2.16)$$

$$-\boldsymbol{\tau}_j \cdot (\mathbb{T}(\mathbf{u}_c, p_c) \cdot \mathbf{n}_c) = \frac{\alpha \nu \sqrt{d}}{\sqrt{\text{trace}(\Pi)}} \boldsymbol{\tau}_j \cdot \mathbf{u}_c, \quad (2.17)$$

FIGURE 1. A sketch of the porous median domain  $\Omega_m$ , fluid domain  $\Omega_c$ , and the interface  $\Gamma$ .

where  $\tau_j$  ( $j = 1, \dots, d-1$ ) are the unit tangential vectors along the interface and  $\Pi$  is the permeability of the porous media,  $\Pi = \mathbb{K}\nu(\phi_c)$  [14, 22, 49]. Equations (2.11)–(2.14) describe the continuity of the phase variable, chemical potential function as well as their derivative with respect to normal direction [49, 50]. Equation (2.15) stands for the continuity of velocity in normal direction and guarantees the mass conservation. Equation (2.16) is known as Lions interface condition describing the balance of forces [28, 49, 51] arising from the momentum equation written in divergence form [20, 32]. Equation (2.17) is the well-known Beavers–Joseph–Saffman–Jones (BJSJ) interface condition [7, 16].

We assume that the coupled CHNSD system satisfies the following boundary conditions

$$\mathbf{u}_c|_{\Gamma_c} = 0, \quad \nabla\phi_c \cdot \mathbf{n}_c|_{\Gamma_c} = 0, \quad M_c \nabla w_c \cdot \mathbf{n}_c|_{\Gamma_c} = 0, \quad (2.18)$$

$$\mathbf{u}_m \cdot \mathbf{n}_m|_{\Gamma_m} = 0, \quad \nabla\phi_m \cdot \mathbf{n}_m|_{\Gamma_m} = 0, \quad M_m \nabla w_m \cdot \mathbf{n}_m|_{\Gamma_m} = 0, \quad (2.19)$$

where  $\Gamma_c = \partial\Omega_c \setminus \Gamma$  and  $\Gamma_m = \partial\Omega_m \setminus \Gamma$ , as well as initial conditions

$$\phi_j(0, x, y) = \phi_j^0(x, y), \quad j = c, m, \quad \mathbf{u}_c(0, x, y) = \mathbf{u}_c^0(x, y). \quad (2.20)$$

Without loss of generality,  $\mathbb{K}$  is assumed to be a bounded, symmetric and uniformly positive definite matrix throughout the paper. For the sake of simplicity, we ignore the body force term  $\rho\mathbf{g}$  as presented in (2.2) and (2.7) in the rest part of this paper except otherwise specified.

Following the idea in [45, 79], denoting  $\sigma = \sqrt{\rho}$ , we deduce

$$\sigma \frac{\partial(\sigma \mathbf{u}_c)}{\partial t} = \rho \frac{\partial \mathbf{u}_c}{\partial t} + \frac{1}{2} \frac{\partial \rho}{\partial t} \mathbf{u}_c = \rho \frac{\partial \mathbf{u}_c}{\partial t} - \frac{1}{2} \nabla \cdot (\rho \mathbf{u}_c) \mathbf{u}_c$$

by using the mass conservation equation

$$\frac{\partial \rho}{\partial t} + \nabla \cdot (\rho \mathbf{u}_c) = 0. \quad (2.21)$$

Then, we can rewrite (2.7) as

$$\sigma \frac{\partial(\sigma \mathbf{u}_c)}{\partial t} + \rho(\mathbf{u}_c \cdot \nabla) \mathbf{u}_c - \nabla \cdot \mathbb{T}(\mathbf{u}_c, p_c) - w_c \nabla \phi_c + \frac{1}{2} \nabla \cdot (\rho \mathbf{u}_c) \mathbf{u}_c = 0. \quad (2.22)$$

The mass conservation (2.21) implies

$$\begin{aligned}
\frac{d}{dt} \left( \rho, \frac{|\mathbf{u}_c|^2}{2} \right) &= \left( \rho \frac{\partial \mathbf{u}_c}{\partial t}, \mathbf{u}_c \right) + \left( \rho_t, \frac{|\mathbf{u}_c|^2}{2} \right) \\
&= \left( \rho \frac{\partial \mathbf{u}_c}{\partial t}, \mathbf{u}_c \right) - \left( \nabla \cdot (\rho \mathbf{u}_c), \frac{|\mathbf{u}_c|^2}{2} \right) \\
&= \left( \rho \frac{\partial \mathbf{u}_c}{\partial t}, \mathbf{u}_c \right) + (\rho \mathbf{u}_c \cdot \nabla \mathbf{u}_c, \mathbf{u}_c) - \frac{1}{2} \int_{\Gamma} \rho (\mathbf{u}_c \cdot \mathbf{u}_c) (\mathbf{u}_c \cdot \mathbf{n}_c) \, ds.
\end{aligned} \tag{2.23}$$

**Remark 2.1.** We follow the idea presented in [38, 78] for (2.21) and (2.22). There is another alternative thermodynamically consistent model for incompressible two-phase flow with different densities [1, 80], which obeys the conservation property

$$\frac{\partial \rho}{\partial t} + \nabla \cdot (\rho \mathbf{u}_c) + \nabla \cdot J = 0, \tag{2.24}$$

where  $J = \frac{\rho_2 - \rho_1}{2} M_c \nabla w_c$ . In this case, one may modify the interface condition (2.16) to obtain energy dissipation law of the two-phase flow since interface conditions are critical for the mathematical modeling of multi-domain two-phase model. In this paper, we focus on the efficient decoupled numerical schemes of CHNSD model associated with (2.21) for different densities.

In order to explicitly handle with the nonlinear term in double well potential, we introduce new variables

$$R_j = \phi_j^2 - 1, \quad j = c, m, \tag{2.25}$$

and then  $f(\phi_j) = \frac{1}{\epsilon} R_j \phi_j$ . Therefore, the Cahn–Hilliard equation in matrix and conduit can be transformed into the following equivalent system:

$$\frac{\partial \phi_j}{\partial t} + \mathbf{u}_j \cdot \nabla \phi_j - \nabla \cdot (M_j \nabla w_j) = 0, \tag{2.26}$$

$$w_j + \gamma \epsilon \Delta \phi_j - \frac{\gamma}{\epsilon} R_j \phi_j = 0, \tag{2.27}$$

$$\frac{\partial R_j}{\partial t} = 2 \phi_j \frac{\partial \phi_j}{\partial t}. \tag{2.28}$$

## 2.2. The weak formulation

In this subsection, the weak formulation is presented for the CHNSD model system (2.2)–(2.17). We will use the Sobolev space  $H^m(\Omega)$  associated with norm  $\|\cdot\|_m$ , and the space  $H_0^m(\Omega) = \{v \in H^m(\Omega) : v|_{\partial\Omega} = 0\}$ , where  $m$  is a nonnegative integer. We use  $\|\cdot\|$  and  $\|\cdot\|_\infty$  to denote the  $L^2$  norm and the  $L^\infty$  norm, respectively. We consider a Hilbert space  $\dot{H}^1(\Omega_j) = H^1(\Omega_j) \cap \dot{L}^2(\Omega_j)$ ,  $j = c, m$ , where  $\dot{L}^2(\Omega_j)$  is defined as follows

$$\dot{L}^2(\Omega_j) := \left\{ v \in L^2(\Omega_j) : \int_{\Omega_j} v \, d\mathbf{x} = 0 \right\}. \tag{2.29}$$

These basic spaces are then used to define the following spaces:

$$\begin{aligned}
\mathbf{X}_c &= \left\{ \mathbf{v} \in [H^1(\Omega_c)]^d \mid \mathbf{v} = 0 \text{ on } \Gamma_c \right\}, \\
\mathbf{X}_m &= \left\{ \mathbf{v} \in [H^1(\Omega_m)]^d \mid \mathbf{v} \cdot \mathbf{n}_m = 0 \text{ on } \Gamma_m \right\}, \\
Q_m &= \dot{H}^1(\Omega_m), \quad Q_c = H^1(\Omega_c),
\end{aligned}$$

$$\begin{aligned}\mathbf{X}_{j,\text{div}} &= \{\mathbf{v} \in X_j \mid \nabla \cdot \mathbf{v} = 0\}, \\ Y_j &= H^1(\Omega_j), \quad j = c, m.\end{aligned}$$

We use  $(\cdot, \cdot)$  to denote the  $L^2$  inner product on the subdomain  $\Omega_j, j = c, m$ , and use  $\langle \cdot, \cdot \rangle$  to denote the  $L^2$  inner product on the interface  $\Gamma$ . Also, we use  $P_\tau$  to denote the projection onto the tangent space on  $\Gamma$ , i.e.,  $P_\tau \mathbf{u} = \sum_{j=1}^{d-1} (\mathbf{u} \cdot \boldsymbol{\tau}_j) \boldsymbol{\tau}_j$ .

Using the interface conditions (2.11)–(2.17) and the IEQ approach, we can obtain the following weak form for the reformulated CHNSD system: find

$$(p_m, \phi_m, w_m, \mathbf{u}_c, p_c, \phi_c, w_c) \in (Q_m, Y_m, Y_m, \mathbf{X}_c, Q_c, Y_c, Y_c)$$

such that

$$(\mathbb{K} \nabla p_m, \nabla q) - (\mathbb{K} w_m \nabla \phi_m, \nabla q) - \langle \mathbf{u}_c \cdot \mathbf{n}_c, q \rangle = 0, \quad \forall q \in Q_m, \quad (2.30)$$

$$\left( \frac{\partial \phi_m}{\partial t}, \psi \right) + (\mathbf{u}_m \cdot \nabla \phi_m, \psi) + (M_m \nabla w_m, \nabla \psi) + \langle M_c \nabla w_c \cdot \mathbf{n}_c, \psi \rangle + \langle \phi_m - \phi_c, \psi \rangle = 0, \quad \forall \psi \in Y_m, \quad (2.31)$$

$$(w_m, \omega) - \gamma \epsilon (\nabla \phi_m, \nabla \omega) - \frac{\gamma}{\epsilon} (R_m \phi_m, \omega) - \gamma \epsilon \langle \nabla \phi_c \cdot \mathbf{n}_c, \omega \rangle + \langle w_m - w_c, \omega \rangle = 0, \quad \forall \omega \in Y_m, \quad (2.32)$$

$$\begin{aligned} & \left( \sigma \frac{\partial (\sigma \mathbf{u}_c)}{\partial t}, \mathbf{v} \right) + (\rho (\mathbf{u}_c \cdot \nabla) \mathbf{u}_c, \mathbf{v}) + (2\nu \mathbb{D}(\mathbf{u}_c), \mathbb{D}(\mathbf{v})) - (p_c, \nabla \cdot \mathbf{v}) \\ & - (w_c \nabla \phi_c, \mathbf{v}) + \frac{1}{2} (\nabla \cdot (\rho \mathbf{u}_c) \mathbf{u}_c, \mathbf{v}) + \left\langle p_m - \frac{\rho}{2} |\mathbf{u}_c|^2, \mathbf{v} \cdot \mathbf{n}_c \right\rangle \\ & + \frac{\alpha \sqrt{d}}{\sqrt{\text{trace}(\Pi)}} \langle \nu P_\tau \mathbf{u}_c, P_\tau \mathbf{v} \rangle = 0, \quad \forall \mathbf{v} \in \mathbf{X}_c, \end{aligned} \quad (2.33)$$

$$(\nabla \cdot \mathbf{u}_c, q) = 0, \quad \forall q \in Q_c, \quad (2.34)$$

$$\left( \frac{\partial \phi_c}{\partial t}, \psi \right) + (\mathbf{u}_c \cdot \nabla \phi_c, \psi) + (M_c \nabla w_c, \nabla \psi) + \langle M_m \nabla w_m \cdot \mathbf{n}_m, \psi \rangle + \langle \phi_c - \phi_m, \psi \rangle = 0, \quad \forall \psi \in Y_c, \quad (2.35)$$

$$(w_c, \omega) - \gamma \epsilon (\nabla \phi_c, \nabla \omega) - \frac{\gamma}{\epsilon} (R_c \phi_c, \omega) - \gamma \epsilon \langle \nabla \phi_m \cdot \mathbf{n}_m, \omega \rangle + \langle w_c - w_m, \omega \rangle = 0, \quad \forall \omega \in Y_c, \quad (2.36)$$

$$\left( \frac{\partial R_j}{\partial t}, \chi \right) = 2 \left( \phi_j \frac{\partial \phi_j}{\partial t}, \chi \right), \quad \forall \chi \in Y_j, \quad (2.37)$$

where  $t \in [0, T]$ ,  $T > 0$ ,  $\mathbf{u}_m \in L^\infty(0, T; [L^2(\Omega_m)]^d) \cap L^2(0, T; \mathbf{X}_m)$ ,  $\mathbf{u}_c \in L^\infty(0, T; [L^2(\Omega_c)]^d) \cap L^2(0, T; \mathbf{X}_{c,\text{div}})$ ,  $\frac{\partial \mathbf{u}_c}{\partial t} \in L^2(0, T; \mathbf{X}'_{c,\text{div}})$ ,  $p_j \in L^2(0, T; Q_j)$ ,  $\phi_j \in L^\infty(0, T; Y_j) \cap L^2(0, T; H^3(\Omega_j))$ ,  $\frac{\partial \phi_j}{\partial t} \in L^2(0, T; Y'_j)$ ,  $w_j \in L^2(0, T; Y_j)$ , and  $j = \{c, m\}$ . Here, by (2.2), we have assumed that  $\mathbf{u}_m$  can be obtained as follows:

$$(\mathbf{u}_m, \mathbf{v}) = (\mathbb{K}(-\nabla p_m + w_m \nabla \phi_m), \mathbf{v}), \quad \forall \mathbf{v} \in \mathbf{X}_m. \quad (2.38)$$

We follow the idea in [39] to solve the two Cahn–Hilliard equations on  $\Omega_m$  and  $\Omega_c$  separately with appropriate treatment for the phase interface conditions (2.11)–(2.14). This is in contrast to the idea in [27], where a single Cahn–Hilliard equation was solved over the whole domain  $\Omega$ . The other three interface conditions (2.15)–(2.17) are utilized in the traditional way for the single-phase Navier–Stokes–Darcy model [4, 22, 32, 51, 75].

**Lemma 2.2.** *Assume  $\phi_j \in H^2(\Omega_j)$ ,  $w_j \in H^2(\Omega_j)$ ,  $\mathbf{u}_c \in [H^2(\Omega_c)]^d$ ,  $\mathbf{u}_m \in [H^1(\Omega_m)]^d$ . Then the weak formulation (2.30)–(2.37) and the CHNSD model (2.2)–(2.17) are equivalent. In particular, the solution*

$$(p_m, \phi_m, w_m, \mathbf{u}_c, p_c, \phi_c, w_c) \in (Q_m, Y_m, Y_m, \mathbf{X}_c, Q_c, Y_c, Y_c)$$

*of the weak formulation (2.30)–(2.37) satisfies the strong interface conditions (2.11), (2.12), and the weak interface conditions as follows, for  $j = c, m$ ,*

$$\langle \mathbf{u}_c \cdot \mathbf{n}_c + \mathbf{u}_m \cdot \mathbf{n}_m, q \rangle = 0, \quad \forall q \in Y_m, \quad (2.39)$$

$$\langle M_m \nabla w_m \cdot \mathbf{n}_m + M_c \nabla w_c \cdot \mathbf{n}_c, \psi \rangle = 0, \quad \forall \psi \in Y_j, \quad (2.40)$$

$$\langle \nabla \phi_c \cdot \mathbf{n}_c + \nabla \phi_m \cdot \mathbf{n}_m, \omega \rangle = 0, \quad \forall \omega \in Y_j, \quad (2.41)$$

$$\begin{aligned} & \left\langle p_m - \frac{\rho}{2} |\mathbf{u}_c|^2 - (\mathbb{T}(\mathbf{u}_c, p_c) \cdot \mathbf{n}_c) \cdot \mathbf{n}_c, \mathbf{v} \cdot \mathbf{n}_c \right\rangle \\ & + \left\langle (\mathbb{T}(\mathbf{u}_c, p_c) \cdot \mathbf{n}_c) \cdot \boldsymbol{\tau}_j + \frac{\alpha \nu \sqrt{d}}{\sqrt{\text{trace}(\Pi)}} (\mathbf{u}_c \cdot \boldsymbol{\tau}_j), \mathbf{v} \cdot \boldsymbol{\tau}_j \right\rangle = 0. \end{aligned} \quad (2.42)$$

*Proof.* On one hand, one can easily derive the weak formulation (2.30)–(2.37) from the CHNSD system (2.2)–(2.17), by utilizing the Green's formula and the interface/boundary conditions. On the other hand, one can obtain (2.2)–(2.10) after applying integration by parts to the weak formulation while choosing the test functions satisfying  $q \in H_0^1(\Omega_j)$ ,  $\psi \in H_0^1(\Omega_j)$ ,  $\omega \in H_0^1(\Omega_j)$ ,  $\mathbf{v} \in [H_0^1(\Omega_c)]^d$  for  $j = c, m$ .

In the following, we focus on the equivalence on the interface. First, applying integration by parts and using (2.2) and boundary condition for  $\mathbf{u}_m$  in (2.19), one can easily conduct (2.39) from (2.30).

Second, similar to the proof of (2.39), using integration by parts and (2.18), we can derive (2.42) from (2.33).

Next, we present the proof that the continuous interface conditions (2.11), (2.12) and (2.40), (2.41) hold in the variational formulation when restricted to the interface  $\Gamma$ . Recall that the weak solution satisfies (2.2)–(2.5) and (2.7)–(2.10). Using (2.31), (2.32), (2.35), (2.36), and integration by parts, we can obtain

$$\langle \phi_m - \phi_c, \psi \rangle + \langle M_m \nabla w_m \cdot \mathbf{n}_m + M_c \nabla w_c \cdot \mathbf{n}_c, \psi \rangle = 0, \quad \forall \psi \in Y_m, \quad (2.43)$$

$$\langle w_m - w_c, \omega \rangle + \gamma \epsilon \langle \nabla \phi_c \cdot \mathbf{n}_c + \nabla \phi_m \cdot \mathbf{n}_m, \omega \rangle = 0, \quad \forall \omega \in Y_m, \quad (2.44)$$

$$\langle \phi_c - \phi_m, \psi \rangle + \langle M_m \nabla w_m \cdot \mathbf{n}_m + M_c \nabla w_c \cdot \mathbf{n}_c, \psi \rangle = 0, \quad \forall \psi \in Y_c, \quad (2.45)$$

$$\langle w_c - w_m, \omega \rangle + \gamma \epsilon \langle \nabla \phi_m \cdot \mathbf{n}_m + \nabla \phi_c \cdot \mathbf{n}_c, \omega \rangle = 0, \quad \forall \omega \in Y_c. \quad (2.46)$$

Choosing  $\psi = \phi_m - \phi_c$  in (2.43) and (2.45), and subtracting these two equations, we have

$$\langle \phi_m - \phi_c, \phi_m - \phi_c \rangle = 0,$$

namely  $\phi_m = \phi_c$ . Hence we obtain (2.11). Choosing  $\omega = w_c - w_m$  in (2.44) and (2.46), and subtracting these two equations, we have

$$\langle w_m - w_c, w_m - w_c \rangle = 0.$$

Then, we obtain  $w_m = w_c$ , namely, the interface condition (2.12).

Plugging (2.11) and (2.12) into (2.43) and (2.44), we obtain (2.40) and (2.41). Hence we complete the proof of Lemma 2.2.  $\square$

### 2.3. A dissipative energy law

For the solution to the coupled CHNSD system, we consider its energy in the following form:

$$E(t) = \frac{1}{2} \|\sigma \mathbf{u}_c\|^2 + \gamma \left[ \frac{\epsilon}{2} \|\nabla \phi_c\|^2 + \frac{1}{4\epsilon} \|R_c\|^2 \right] + \gamma \left[ \frac{\epsilon}{2} \|\nabla \phi_m\|^2 + \frac{1}{4\epsilon} \|R_m\|^2 \right] \quad (2.47)$$

which will not grow as suggested by the theorem below.

**Theorem 2.3.** *The smooth solution  $(\mathbf{u}_m, \mathbf{u}_c, \phi_m, \phi_c)$  of the coupled CHNSD system with different densities (2.2)–(2.20) satisfies the following energy dissipation law*

$$\frac{d}{dt} E(t) = -\mathcal{D}(t), \quad (2.48)$$

where  $\mathcal{D}$  is defined by

$$\mathcal{D}(t) = \left\| \sqrt{2\nu} \mathbb{D}(\mathbf{u}_c) \right\|^2 + \left\| \sqrt{\mathbb{K}^{-1}} \mathbf{u}_m \right\|^2 + M_c \|\nabla w_c\|^2 + M_m \|\nabla w_m\|^2 + \frac{\alpha \sqrt{d}}{\sqrt{\text{trace}(\Pi)}} \langle \nu P_\tau \mathbf{u}_c, P_\tau \mathbf{u}_c \rangle. \quad (2.49)$$



*Proof.* We firstly consider the conduit part. By letting  $\mathbf{v} = \mathbf{u}_c$ ,  $q = p_c$ ,  $\psi = w_c$ ,  $\omega = -\frac{\partial \phi_c}{\partial t}$  in (2.33)–(2.36),  $\chi = \frac{\gamma}{2\epsilon} R_c$  in (2.37), applying the interface conditions (2.11) and (2.12), and summing up the resultants together, we have

$$\begin{aligned} & \frac{1}{2} \frac{d}{dt} \|\sigma \mathbf{u}_c\|^2 + \gamma \left[ \frac{\epsilon}{2} \frac{d}{dt} \|\nabla \phi_c\|^2 + \frac{1}{4\epsilon} \frac{d}{dt} \|R_c\|^2 \right] + (\rho(\mathbf{u}_c \cdot \nabla) \mathbf{u}_c, \mathbf{u}_c) + \frac{1}{2} (\nabla \cdot (\rho \mathbf{u}_c) \mathbf{u}_c, \mathbf{u}_c) \\ & + \left\| \sqrt{2\nu} \mathbb{D}(\mathbf{u}_c) \right\|^2 + M_c \|\nabla w_c\|^2 + \frac{\alpha \sqrt{d}}{\sqrt{\text{trace}(\Pi)}} \langle \nu P_\tau \mathbf{u}_c, P_\tau \mathbf{u}_c \rangle \\ & + \langle M_m \nabla w_m \cdot \mathbf{n}_m, w_c \rangle + \gamma \epsilon \left\langle \nabla \phi_m \cdot \mathbf{n}_m, \frac{d}{dt} \phi_c \right\rangle + \left\langle \mathbf{u}_c \cdot \mathbf{n}_c, p_m - \frac{\rho}{2} |\mathbf{u}_c|^2 \right\rangle = 0. \end{aligned} \quad (2.50)$$

Using integration by parts we can see

$$((\rho \mathbf{u}_c \cdot \nabla) \mathbf{u}_c, \mathbf{u}_c) + \frac{1}{2} (\nabla \cdot (\rho \mathbf{u}_c) \mathbf{u}_c, \mathbf{u}_c) = \frac{1}{2} \langle \rho \mathbf{u}_c \cdot \mathbf{u}_c, \mathbf{u}_c \cdot \mathbf{n}_c \rangle. \quad (2.51)$$

Applying (2.51) in (2.50) leads to

$$\begin{aligned} & \frac{1}{2} \frac{d}{dt} \|\sigma \mathbf{u}_c\|^2 + \gamma \left[ \frac{\epsilon}{2} \frac{d}{dt} \|\nabla \phi_c\|^2 + \frac{1}{4\epsilon} \frac{d}{dt} \|R_c\|^2 \right] + \left\| \sqrt{2\nu} \mathbb{D}(\mathbf{u}_c) \right\|^2 + M_c \|\nabla w_c\|^2 + \langle \mathbf{u}_c \cdot \mathbf{n}_c, p_m \rangle \\ & + \frac{\alpha \sqrt{d}}{\sqrt{\text{trace}(\Pi)}} \langle \nu P_\tau \mathbf{u}_c, P_\tau \mathbf{u}_c \rangle + \langle M_m \nabla w_m \cdot \mathbf{n}_m, w_c \rangle + \gamma \epsilon \left\langle \nabla \phi_m \cdot \mathbf{n}_m, \frac{d}{dt} \phi_c \right\rangle = 0. \end{aligned} \quad (2.52)$$

Then, for the matrix part, choosing  $q = p_m$  in (2.30) and  $\psi = w_m$  in (2.31), adding the resultants together and applying (2.38), we obtain

$$\left( \frac{\partial \phi_m}{\partial t}, w_m \right) + (\mathbf{u}_m \cdot \nabla \phi_m, w_m) - (\mathbf{u}_m, \nabla p_m) + M_m \|\nabla w_m\|^2 + \langle M_c \nabla w_c \cdot \mathbf{n}_c, w_m \rangle - \langle \mathbf{u}_c \cdot \mathbf{n}_c, p_m \rangle = 0. \quad (2.53)$$

Using  $\mathbf{v} = \mathbf{u}_m$  in (2.38) yields

$$\left\| \sqrt{\mathbb{K}^{-1}} \mathbf{u}_m \right\|^2 = -(\nabla p_m, \mathbf{u}_m) + (w_m \nabla \phi_m, \mathbf{u}_m). \quad (2.54)$$

We add (2.53) and (2.54) to obtain

$$\left( \frac{\partial \phi_m}{\partial t}, w_m \right) + \left\| \sqrt{\mathbb{K}^{-1}} \mathbf{u}_m \right\|^2 + M_m \|\nabla w_m\|^2 + \langle M_c \nabla w_c \cdot \mathbf{n}_c, w_m \rangle - \langle \mathbf{u}_c \cdot \mathbf{n}_c, p_m \rangle = 0. \quad (2.55)$$

By taking  $\omega = -\frac{\partial \phi_m}{\partial t}$  in (2.32) and  $\chi = \frac{\gamma}{2\epsilon} R_m$  in (2.37), respectively, and adding (2.55), we derive

$$\begin{aligned} & \gamma \left[ \frac{\epsilon}{2} \frac{d}{dt} \|\nabla \phi_m\|^2 + \frac{1}{4\epsilon} \frac{d}{dt} \|R_m\|^2 \right] + \left\| \sqrt{\mathbb{K}^{-1}} \mathbf{u}_m \right\|^2 + M_m \|\nabla w_m\|^2 \\ & + \langle M_c \nabla w_c \cdot \mathbf{n}_c, w_m \rangle + \gamma \epsilon \left\langle \nabla \phi_c \cdot \mathbf{n}_c, \frac{d}{dt} \phi_m \right\rangle - \langle \mathbf{u}_c \cdot \mathbf{n}_c, p_m \rangle = 0. \end{aligned} \quad (2.56)$$

By adding (2.52) and (2.56), applying the interface conditions (2.11)–(2.14), we obtain (2.48).  $\square$

### 3. ENERGY-STABLE TIME-STEPPING METHODS

In this section, we present and analyze a partially decoupled time-stepping scheme and a fully decoupled scheme for solving the CHNSD system (2.30)–(2.37). First, for a preparation and by following the ideas in [69], we have the following lemma for estimating the interface terms.

**Lemma 3.1.** *There exists a constant  $C$  such that, for  $\mathbf{v} \in \mathbf{X}_c$ ,  $q_m \in Q_m$*

$$|\langle \mathbf{v} \cdot \mathbf{n}_c, q_m \rangle| \leq C \|\mathbf{v}\|_{\mathbf{X}_{\text{div}}} \|\nabla q_m\|, \quad (3.1)$$

where  $\|\mathbf{v}\|_{\mathbf{X}_{\text{div}}}^2 = \|\mathbf{v}\|^2 + \|\nabla \cdot \mathbf{v}\|^2$ . If  $\mathbf{v}$  satisfy

$$(\nabla \cdot \mathbf{v}, q_m) = 0, \quad \forall q_m \in Q_m, \quad (3.2)$$

then

$$|\langle \mathbf{v} \cdot \mathbf{n}_c, q_m \rangle| \leq C \|\mathbf{v}\| \|\nabla q_m\|. \quad (3.3)$$

Also, in discussions from now on, we let the time step size be  $\Delta t = t_{n+1} - t_n = \frac{T}{M}$ ,  $t_n$  be the  $n$ th discrete time level, and  $M = \frac{T}{\Delta t}$ .

#### 3.1. A partially decoupled scheme based on the pressure correction method

Following the works in [39], we decouple CHNSD system into two subsystem by the modification of the interface conditions. Then we use a stabilization technique to decouple the CHNS system and the CHD system into two subsystems, respectively. Consequently, we obtain four sub-systems. Finally, we employ the pressure projection correction method [38, 78] in dealing with Navier–Stokes equations to derive a linearized system with energy-preserving property. These essential components help us obtain a decoupled, linearized, and energy stable scheme for the temporal discretization as follows.

**Step 1.** Find  $(\phi_m^{n+1}, w_m^{n+1}) \in Y_m \times Y_m$ , such that

$$\begin{aligned} & \left( \frac{\phi_m^{n+1} - \phi_m^n}{\Delta t}, \psi \right) - (\mathbb{K} \nabla p_m^n \cdot \nabla \phi_m^n, \psi) + (\mathbb{K} w_m^{n+1} \nabla \phi_m^n \cdot \nabla \phi_m^n, \psi) \\ & + (M_m \nabla w_m^{n+1}, \nabla \psi) + \langle M_c \nabla w_c^n \cdot \mathbf{n}_c, \psi \rangle + \langle \phi_m^n - \phi_c^n, \psi \rangle = 0, \quad \forall \psi \in Y_m, \end{aligned} \quad (3.4)$$

$$\begin{aligned} & (w_m^{n+1}, \omega) - \gamma \epsilon (\nabla \phi_m^{n+1}, \nabla \omega) - \frac{\gamma}{\epsilon} (R_m^n \phi_m^n, \omega) - \frac{S\gamma}{\epsilon} (\phi_m^{n+1} - \phi_m^n, \omega) \\ & - \gamma \epsilon \langle \nabla \phi_c^n \cdot \mathbf{n}_c, \omega \rangle + \langle w_m^n - w_c^n, \omega \rangle = 0, \quad \forall \omega \in Y_m, \end{aligned} \quad (3.5)$$

where we have used

$$\mathbf{u}_m^{n+1} = -\mathbb{K} \nabla p_m^n + \mathbb{K} w_m^{n+1} \nabla \phi_m^n. \quad (3.6)$$

**Step 2.** Find  $p_m^{n+1} \in Q_m$ , such that

$$(\mathbb{K} \nabla p_m^{n+1}, \nabla q) - (\mathbb{K} w_m^{n+1} \nabla \phi_m^n, \nabla q) - \langle \mathbf{u}_c^n \cdot \mathbf{n}_c, q \rangle + \beta \Delta t (\nabla p_m^{n+1}, \nabla q) = 0, \quad \forall q \in Q_m. \quad (3.7)$$

**Step 3.** Find  $(\phi_c^{n+1}, w_c^{n+1}) \in Y_c \times Y_c$ , such that

$$\begin{aligned} & \left( \frac{\phi_c^{n+1} - \phi_c^n}{\Delta t}, \psi \right) + (\mathbf{u}_{c*}^n \cdot \nabla \phi_c^n, \psi) + (M_c \nabla w_c^{n+1}, \nabla \psi) + \langle M_m \nabla w_m^n \cdot \mathbf{n}_m, \psi \rangle \\ & + \langle \phi_c^{n+1} - \phi_m^{n+1}, \psi \rangle = 0, \quad \forall \psi \in Y_c, \end{aligned} \quad (3.8)$$

$$(w_c^{n+1}, \omega) - \gamma \epsilon (\nabla \phi_c^{n+1}, \nabla \omega) - \frac{\gamma}{\epsilon} (R_c^n \phi_c^n, \omega) - \frac{S\gamma}{\epsilon} (\phi_c^{n+1} - \phi_c^n, \omega) - \gamma \epsilon \langle \nabla \phi_m^n \cdot \mathbf{n}_m, \omega \rangle$$

$$+ \langle w_c^{n+1} - w_m^{n+1}, \omega \rangle = 0. \quad \forall \omega \in Y_c, \quad (3.9)$$

where  $\mathbf{u}_{c*}^n$  is given by

$$\mathbf{u}_{c*}^n = \mathbf{u}_c^n + \frac{1}{\rho^n} \Delta t w_c^{n+1} \nabla \phi_c^n. \quad (3.10)$$

**Step 4.** Find  $(\tilde{\mathbf{u}}_c^{n+1}, \mathbf{u}_c^{n+1}, p_c^{n+1}) \in \mathbf{X}_c \times \mathbf{X}_c \times Q_c$ , such that

$$\begin{aligned} & \left( \rho^n \frac{\tilde{\mathbf{u}}_c^{n+1} - \mathbf{u}_c^n}{\Delta t}, \mathbf{v} \right) + \left( \rho^n (\mathbf{u}_c^n \cdot \nabla) \tilde{\mathbf{u}}_c^{n+1}, \mathbf{v} \right) + \left( 2\nu^n \mathbb{D}(\tilde{\mathbf{u}}_c^{n+1}), \mathbb{D}(\mathbf{v}) \right) \\ & - (w_c^{n+1} \nabla \phi_c^n, \mathbf{v}) + \frac{1}{2} \left( \tilde{\mathbf{u}}_c^{n+1} \frac{\rho^{n+1} - \rho^n}{\Delta t}, \mathbf{v} \right) + \frac{1}{2} \left( \nabla \cdot (\rho^n \mathbf{u}_c^n) \tilde{\mathbf{u}}_c^{n+1}, \mathbf{v} \right) \\ & + \langle p_m^{n+1} - p_c^{n+1}, \mathbf{v} \cdot \mathbf{n}_c \rangle - \frac{1}{2} \langle \rho^n \mathbf{u}_c^n \cdot \tilde{\mathbf{u}}_c^{n+1}, \mathbf{v} \cdot \mathbf{n}_c \rangle \\ & + \frac{\alpha \sqrt{d}}{\sqrt{\text{trace}(\Pi)}} \langle \nu^n P_\tau \tilde{\mathbf{u}}_c^{n+1}, P_\tau \mathbf{v} \rangle = 0, \quad \forall \mathbf{v} \in \mathbf{X}_c. \end{aligned} \quad (3.11)$$

$$\left( \rho^{n+1} \frac{\mathbf{u}_c^{n+1} - \tilde{\mathbf{u}}_c^{n+1}}{\Delta t}, \mathbf{v} \right) + (\nabla p_c^{n+1}, \mathbf{v}) = 0, \quad \forall \mathbf{v} \in \mathbf{X}_c, \quad (3.12)$$

$$(\nabla \cdot \mathbf{u}_c^{n+1}, q) = 0, \quad \forall q \in Q_c. \quad (3.13)$$

**Step 5.** Find  $R_c^{n+1} \in Y_c$  and  $R_m^{n+1} \in Y_m$ , such that

$$\left( \frac{R_c^{n+1} - R_c^n}{\Delta t}, \chi \right) = 2 \left( \phi_c^n \frac{\phi_c^{n+1} - \phi_c^n}{\Delta t}, \chi \right), \quad \forall \chi \in Y_c, \quad (3.14)$$

$$\left( \frac{R_m^{n+1} - R_m^n}{\Delta t}, \chi \right) = 2 \left( \phi_m^n \frac{\phi_m^{n+1} - \phi_m^n}{\Delta t}, \chi \right), \quad \forall \chi \in Y_m. \quad (3.15)$$

**Remark 3.2.** In the scheme above, we imposed the following interface condition for the intermediate velocity  $\tilde{\mathbf{u}}_c^{n+1}$ :

$$\tilde{\mathbf{u}}_c^{n+1} \cdot \mathbf{n}_c|_\Gamma = \mathbf{u}_c^{n+1} \cdot \mathbf{n}_c|_\Gamma. \quad (3.16)$$

**Remark 3.3.** The two extra terms  $\frac{S\gamma}{\epsilon}(\phi_m^{n+1} - \phi_m^n)$  and  $\frac{S\gamma}{\epsilon}(\phi_c^{n+1} - \phi_c^n)$  in (3.5) and (3.9), respectively, are stabilizers usually employed to enhance the stability and maintain the resolution with a positive stabilizing parameter  $S$ .

**Remark 3.4.** The term  $\beta(\nabla p_m^{n+1}, \nabla q)$  in (3.7) is introduced to ensure the stability of numerical scheme with respect to the positive parameter  $\beta$ .

**Theorem 3.5.** Assume that the stabilized parameter  $\beta$  is chosen to be large enough. Then The time-stepping scheme (3.4)–(3.15) is unconditionally stable, namely  $(\mathbf{u}_c^{n+1}, p_m^{n+1}, p_c^{n+1}, \phi_m^{n+1}, \phi_c^{n+1}, R_m^{n+1}, R_c^{n+1})$  defined by (3.4)–(3.15) satisfies the energy dissipation law:

$$\mathcal{E}_{pd}^{n+1} - \mathcal{E}_{pd}^n \leq -\mathcal{D}_{pd}^{n+1}, \quad (3.17)$$

where  $\mathcal{E}_{pd}^n$  is defined as

$$\mathcal{E}_{pd}^n = \frac{1}{2} \|\sigma^n \mathbf{u}_c^n\|^2 + \gamma \left[ \frac{\epsilon}{2} \|\nabla \phi_c^n\|^2 + \frac{1}{4\epsilon} \|R_c^n\|^2 \right] + \gamma \left[ \frac{\epsilon}{2} \|\nabla \phi_m^n\|^2 + \frac{1}{4\epsilon} \|R_m^n\|^2 \right] + \frac{1}{2} \Delta t \left\| \sqrt{\mathbb{K}} \nabla p_m^n \right\|^2, \quad (3.18)$$

$\mathcal{D}_{pd}^{n+1}$  is given by

$$\begin{aligned} \mathcal{D}_{pd}^{n+1} = & \Delta t \left\| \sqrt{2\nu^n} \mathbb{D}(\tilde{\mathbf{u}}_c^{n+1}) \right\|^2 + \frac{1}{4} \Delta t \left\| \sqrt{\mathbb{K}} \nabla (p_m^{n+1} - p_m^n) \right\|^2 + \frac{\gamma\epsilon}{2} \left\| \nabla \phi_c^{n+1} - \nabla \phi_c^n \right\|^2 + \frac{\gamma\epsilon}{2} \left\| \nabla \phi_m^{n+1} - \nabla \phi_m^n \right\|^2 \\ & + \frac{\gamma}{4\epsilon} \left\| R_c^{n+1} - R_c^n \right\|^2 + \frac{\gamma}{4\epsilon} \left\| R_m^{n+1} - R_m^n \right\|^2 + \frac{S\gamma}{\epsilon} \left\| \phi_c^{n+1} - \phi_c^n \right\|^2 + \frac{S\gamma}{\epsilon} \left\| \phi_m^{n+1} - \phi_m^n \right\|^2 \\ & + \Delta t M_c \left\| \nabla w_c^{n+1} \right\|^2 + \Delta t M_m \left\| \nabla w_m^{n+1} \right\|^2 + \Delta t \frac{\alpha\sqrt{d}}{\sqrt{\text{trace}(\Pi)}} \langle \nu^n P_\tau \mathbf{u}_c^{n+1}, P_\tau \mathbf{u}_c^{n+1} \rangle. \end{aligned} \quad (3.19)$$

*Proof.* We first consider the conduit part. By (2.51), we have

$$\left( (\rho^n \mathbf{u}_c^n \cdot \nabla) \tilde{\mathbf{u}}_c^{n+1}, \tilde{\mathbf{u}}_c^{n+1} \right) + \frac{1}{2} \left( \nabla \cdot (\rho^n \mathbf{u}_c^n) \tilde{\mathbf{u}}_c^{n+1}, \tilde{\mathbf{u}}_c^{n+1} \right) = \frac{1}{2} \left\langle \rho^n \mathbf{u}_c^n \cdot \tilde{\mathbf{u}}_c^{n+1}, \tilde{\mathbf{u}}_c^{n+1} \cdot \mathbf{n}_c \right\rangle. \quad (3.20)$$

By taking the test function  $\mathbf{v} = \Delta t \tilde{\mathbf{u}}_c^{n+1}$  in (3.11),  $\mathbf{v} = \Delta t \mathbf{u}_c^{n+1}$  in (3.12) and  $q = \Delta t p_c^{n+1}$  in (3.13), then adding these two equations, combining the result with (3.20), the interface condition (3.16), and the identity

$$2a(a-b) = a^2 - b^2 + (a-b)^2, \quad (3.21)$$

we obtain

$$\begin{aligned} & \frac{1}{2} \left[ \left\| \sigma^{n+1} \mathbf{u}_c^{n+1} \right\|^2 - \left\| \sigma^n \mathbf{u}_{c\star}^n \right\|^2 + \left\| \sigma^n (\tilde{\mathbf{u}}_c^{n+1} - \mathbf{u}_{c\star}^n) \right\|^2 + \left\| \sigma^{n+1} (\mathbf{u}_c^{n+1} - \tilde{\mathbf{u}}_c^{n+1}) \right\|^2 \right] \\ & + \Delta t \left\| \sqrt{2\nu^n} \mathbb{D}(\tilde{\mathbf{u}}_c^{n+1}) \right\|^2 + \Delta t \langle \mathbf{u}_c^{n+1} \cdot \mathbf{n}_c, p_m^{n+1} \rangle + \Delta t \frac{\alpha\sqrt{d}}{\sqrt{\text{trace}(\Pi)}} \langle \nu^n P_\tau \tilde{\mathbf{u}}_c^{n+1}, P_\tau \tilde{\mathbf{u}}_c^{n+1} \rangle = 0, \end{aligned} \quad (3.22)$$

where the Green's formula is used for term  $(\nabla p_c^{n+1}, \mathbf{u}_{c\star}^{n+1}) = -(p_c^{n+1}, \nabla \cdot \mathbf{u}_{c\star}^{n+1}) + \langle p_c^{n+1}, \mathbf{u}_{c\star}^{n+1} \cdot \mathbf{n}_c \rangle$ .

In order to deal with the  $\left\| \sigma^n \mathbf{u}_{c\star}^n \right\|^2$  term, we rewrite (3.10) as

$$\frac{\rho^n (\mathbf{u}_{c\star}^n - \mathbf{u}_c^n)}{\Delta t} = w_c^{n+1} \nabla \phi_c^n, \quad (3.23)$$

and take the inner product of (3.23) with  $\Delta t \mathbf{u}_{c\star}^n$ . Then, by the identity (3.21), we obtain

$$\frac{1}{2} \left[ \left\| \sigma^n \mathbf{u}_{c\star}^n \right\|^2 - \left\| \sigma^n \mathbf{u}_c^n \right\|^2 + \left\| \sigma^n (\mathbf{u}_{c\star}^n - \mathbf{u}_c^n) \right\|^2 \right] = \Delta t (w_c^{n+1} \nabla \phi_c^n, \mathbf{u}_{c\star}^n). \quad (3.24)$$

Letting  $\psi = \Delta t w_c^{n+1}$  in (3.8), and applying (2.11) and (3.10), we get

$$(\phi_c^{n+1} - \phi_c^n, w_c^{n+1}) + \Delta t (\mathbf{u}_{c\star}^n \cdot \nabla \phi_c^n, w_c^{n+1}) + \Delta t M_c \left\| \nabla w_c^{n+1} \right\|^2 + \Delta t \langle M_m \nabla w_m^n \cdot \mathbf{n}_c, w_c^{n+1} \rangle = 0. \quad (3.25)$$

Then, we use  $\omega = -(\phi_c^{n+1} - \phi_c^n)$  and  $\chi = \frac{\gamma}{2\epsilon} \Delta t R_c^{n+1}$  in (3.9) and (3.14), respectively, and let  $\chi = \frac{\gamma}{\epsilon} \Delta t (\phi_c^{n+1} - \phi_c^n)$  in (3.14), utilize (2.12) and (3.21) to derive

$$\begin{aligned} & - (w_c^{n+1}, \phi_c^{n+1} - \phi_c^n) + \frac{\gamma\epsilon}{2} \left[ \left\| \nabla \phi_c^{n+1} \right\|^2 - \left\| \nabla \phi_c^n \right\|^2 \right] + \frac{\gamma}{4\epsilon} \left[ \left\| R_c^{n+1} \right\|^2 - \left\| R_c^n \right\|^2 \right] + \gamma\epsilon \langle \nabla \phi_m^n \cdot \mathbf{n}_m, \phi_c^{n+1} - \phi_c^n \rangle \\ & + \frac{\gamma\epsilon}{2} \left\| \nabla \phi_c^{n+1} - \nabla \phi_c^n \right\|^2 + \frac{\gamma}{4\epsilon} \left\| R_c^{n+1} - R_c^n \right\|^2 + \frac{S\gamma}{\epsilon} \left\| \phi_c^{n+1} - \phi_c^n \right\|^2 = 0. \end{aligned} \quad (3.26)$$

Adding (3.22), (3.24), (3.25) and (3.26), we get

$$\frac{1}{2} \left[ \left\| \sigma^{n+1} \mathbf{u}_c^{n+1} \right\|^2 - \left\| \sigma^n \mathbf{u}_c^n \right\|^2 \right] + \frac{\gamma\epsilon}{2} \left[ \left\| \nabla \phi_c^{n+1} \right\|^2 - \left\| \nabla \phi_c^n \right\|^2 \right] + \frac{\gamma}{4\epsilon} \left[ \left\| R_c^{n+1} \right\|^2 - \left\| R_c^n \right\|^2 \right]$$

$$\begin{aligned}
& + \frac{1}{2} \left[ \left\| \sigma^n \left( \tilde{\mathbf{u}}_c^{n+1} - \mathbf{u}_{c*}^n \right) \right\|^2 + \left\| \sigma^{n+1} \left( \mathbf{u}_c^{n+1} - \tilde{\mathbf{u}}_c^{n+1} \right) \right\|^2 + \left\| \sigma^n \left( \mathbf{u}_{c*}^n - \mathbf{u}_c^n \right) \right\|^2 \right] \\
& + \Delta t \left\| \sqrt{2\nu^n} \mathbb{D} \left( \tilde{\mathbf{u}}_c^{n+1} \right) \right\|^2 + \Delta t M_c \left\| \nabla w_c^{n+1} \right\|^2 + \frac{\gamma\epsilon}{2} \left\| \nabla \phi_c^{n+1} - \nabla \phi_c^n \right\|^2 \\
& + \frac{\gamma}{4\epsilon} \left\| R_c^{n+1} - R_c^n \right\|^2 + \frac{S\gamma}{\epsilon} \left\| \phi_c^{n+1} - \phi_c^n \right\|^2 + \gamma \epsilon \langle \nabla \phi_m^n \cdot \mathbf{n}_m, \phi_c^{n+1} - \phi_c^n \rangle \\
& + \Delta t \langle M_m \nabla w_m^n \cdot \mathbf{n}_m, w_c^{n+1} \rangle + \Delta t \langle \mathbf{u}_c^{n+1} \cdot \mathbf{n}_c, p_m^{n+1} \rangle \\
& + \Delta t \frac{\alpha \sqrt{d}}{\sqrt{\text{trace}(\Pi)}} \langle \nu^n P_\tau \mathbf{u}_c^{n+1}, P_\tau \mathbf{u}_c^{n+1} \rangle = 0. \tag{3.27}
\end{aligned}$$

Next, we consider the matrix part. Choosing  $\psi = \Delta t w_m^{n+1}$  in (3.4), using (2.11) and (3.6), we derive

$$(\phi_m^{n+1} - \phi_m^n, w_m^{n+1}) + \Delta t (\mathbf{u}_m^{n+1} \cdot \nabla \phi_m^n, w_m^{n+1}) + \Delta t M_m \left\| \nabla w_m^{n+1} \right\|^2 + \Delta t \langle M_c \nabla w_c^n \cdot \mathbf{n}_c, w_m^{n+1} \rangle = 0. \tag{3.28}$$

Taking  $\omega = -(\phi_m^{n+1} - \phi_m^n)$  in (3.5),  $\chi = \frac{\gamma}{2\epsilon} \Delta t R_m^{n+1}$  in (3.15), and then taking the summation, applying (2.12), and (3.21), we obtain

$$\begin{aligned}
& - (w_m^{n+1}, \phi_m^{n+1} - \phi_m^n) + \frac{\gamma\epsilon}{2} \left[ \left\| \nabla \phi_m^{n+1} \right\|^2 - \left\| \nabla \phi_m^n \right\|^2 \right] + \frac{\gamma}{4\epsilon} \left[ \left\| R_m^{n+1} \right\|^2 - \left\| R_m^n \right\|^2 \right] + \gamma \epsilon \langle \nabla \phi_c^n \cdot \mathbf{n}_c, \phi_m^{n+1} - \phi_m^n \rangle \\
& + \frac{\gamma\epsilon}{2} \left\| \nabla \phi_m^{n+1} - \nabla \phi_m^n \right\|^2 + \frac{\gamma}{4\epsilon} \left\| R_m^{n+1} - R_m^n \right\|^2 + \frac{S\gamma}{\epsilon} \left\| \phi_m^{n+1} - \phi_m^n \right\|^2 = 0. \tag{3.29}
\end{aligned}$$

We take the inner product of (3.6) with  $v_h = \Delta t \mathbb{K}^{-1} \mathbf{u}_m^{n+1}$ , let  $q = \Delta t p_m^{n+1}$  in (3.6), and add the resultants together to obtain

$$\begin{aligned}
& \Delta t \left\| \sqrt{\mathbb{K}^{-1}} \mathbf{u}_m^{n+1} \right\|^2 + \frac{1}{2} \Delta t \left[ \left\| \sqrt{\mathbb{K}} \nabla p_m^{n+1} \right\|^2 - \left\| \sqrt{\mathbb{K}} \nabla p_m^n \right\|^2 + \left\| \sqrt{\mathbb{K}} \nabla (p_m^{n+1} - p_m^n) \right\|^2 \right] + \beta \Delta t^2 \left\| \nabla p_m^{n+1} \right\|^2 \\
& - \Delta t (\nabla (p_m^{n+1} - p_m^n), \mathbf{u}_m^{n+1}) - \Delta t (w_m^{n+1} \nabla \phi_m^n, \mathbf{u}_m^{n+1}) - \Delta t \langle \mathbf{u}_c^n \cdot \mathbf{n}_c, p_m^{n+1} \rangle = 0. \tag{3.30}
\end{aligned}$$

Adding (3.28), (3.29) and (3.30), and then applying

$$\Delta t |(\nabla (p_m^{n+1} - p_m^n), \mathbf{u}_m^{n+1})| \leq \Delta t \left\| \sqrt{\mathbb{K}^{-1}} \mathbf{u}_m^{n+1} \right\|^2 + \frac{1}{4} \Delta t \left\| \sqrt{\mathbb{K}} \nabla (p_m^{n+1} - p_m^n) \right\|^2 \tag{3.31}$$

we obtain

$$\begin{aligned}
& \frac{1}{2} \gamma \epsilon \left[ \left\| \nabla \phi_m^{n+1} \right\|^2 - \left\| \nabla \phi_m^n \right\|^2 \right] + \frac{\gamma}{4\epsilon} \left[ \left\| R_m^{n+1} \right\|^2 - \left\| R_m^n \right\|^2 \right] + \frac{1}{2} \Delta t \left[ \left\| \sqrt{\mathbb{K}} \nabla p_m^{n+1} \right\|^2 - \left\| \sqrt{\mathbb{K}} \nabla p_m^n \right\|^2 \right] \\
& \leq -\frac{1}{2} \gamma \epsilon \left\| \nabla \phi_m^{n+1} - \nabla \phi_m^n \right\|^2 - \Delta t M_m \left\| \nabla w_m^{n+1} \right\|^2 - \frac{1}{4} \Delta t \left\| \sqrt{\mathbb{K}} \nabla (p_m^{n+1} - p_m^n) \right\|^2 \\
& - \frac{\gamma}{4\epsilon} \left\| R_m^{n+1} - R_m^n \right\|^2 - \frac{S\gamma}{\epsilon} \left\| \phi_m^{n+1} - \phi_m^n \right\|^2 - \beta \Delta t^2 \left\| \nabla p_m^{n+1} \right\|^2 + \Delta t \langle \mathbf{u}_c^n \cdot \mathbf{n}_c, p_m^{n+1} \rangle \\
& - \gamma \epsilon \langle \nabla \phi_c^n \cdot \mathbf{n}_c, \phi_m^{n+1} - \phi_m^n \rangle - \Delta t \langle M_c \nabla w_c^n \cdot \mathbf{n}_c, w_m^{n+1} \rangle. \tag{3.32}
\end{aligned}$$

Summing up (3.27) and (3.32), and applying Lemma 2.2, we have

$$\begin{aligned}
& \frac{1}{2} \left[ \left\| \sigma^{n+1} \mathbf{u}_c^{n+1} \right\|^2 - \left\| \sigma^n \mathbf{u}_c^n \right\|^2 \right] + \frac{\gamma\epsilon}{2} \left[ \left\| \nabla \phi_c^{n+1} \right\|^2 - \left\| \nabla \phi_c^n \right\|^2 \right] \\
& + \frac{1}{2} \gamma \epsilon \left[ \left\| \nabla \phi_m^{n+1} \right\|^2 - \left\| \nabla \phi_m^n \right\|^2 \right] + \frac{\gamma}{4\epsilon} \left[ \left\| R_c^{n+1} \right\|^2 - \left\| R_c^n \right\|^2 \right] \\
& + \frac{\gamma}{4\epsilon} \left[ \left\| R_m^{n+1} \right\|^2 - \left\| R_m^n \right\|^2 \right] + \frac{1}{2} \Delta t \left[ \left\| \sqrt{\mathbb{K}} \nabla p_m^{n+1} \right\|^2 - \left\| \sqrt{\mathbb{K}} \nabla p_m^n \right\|^2 \right]
\end{aligned}$$

$$\begin{aligned}
&\leq -\frac{1}{2} \left[ \left\| \sigma^n (\tilde{\mathbf{u}}_c^{n+1} - \mathbf{u}_{c*}^n) \right\|^2 + \left\| \sigma^{n+1} (\mathbf{u}_c^{n+1} - \tilde{\mathbf{u}}_c^{n+1}) \right\|^2 + \left\| \sigma^n (\mathbf{u}_{c*}^n - \mathbf{u}_c^n) \right\|^2 \right] \\
&\quad - \Delta t \left\| \sqrt{2\nu^n} \mathbb{D} (\tilde{\mathbf{u}}_c^{n+1}) \right\|^2 - \frac{1}{4} \Delta t \left\| \sqrt{\mathbb{K}} \nabla (p_m^{n+1} - p_m^n) \right\|^2 - \Delta t M_c \left\| \nabla w_c^{n+1} \right\|^2 - \Delta t M_m \left\| \nabla w_m^{n+1} \right\|^2 \\
&\quad - \frac{\gamma\epsilon}{2} \left\| \nabla \phi_c^{n+1} - \nabla \phi_c^n \right\|^2 - \frac{\gamma\epsilon}{2} \left\| \nabla \phi_m^{n+1} - \nabla \phi_m^n \right\|^2 - \frac{\gamma}{4\epsilon} \left\| R_c^{n+1} - R_c^n \right\|^2 - \frac{\gamma}{4\epsilon} \left\| R_m^{n+1} - R_m^n \right\|^2 \\
&\quad - \frac{S\gamma}{\epsilon} \left\| \phi_c^{n+1} - \phi_c^n \right\|^2 - \frac{S\gamma}{\epsilon} \left\| \phi_m^{n+1} - \phi_m^n \right\|^2 - \Delta t \frac{\alpha\sqrt{d}}{\sqrt{\text{trace}(\Pi)}} \langle \nu^n P_\tau \mathbf{u}_c^{n+1}, P_\tau \mathbf{u}_c^{n+1} \rangle \\
&\quad - \beta \Delta t^2 \left\| \nabla p_m^{n+1} \right\|^2 + \Delta t |\langle (\mathbf{u}_c^{n+1} - \mathbf{u}_c^n) \cdot \mathbf{n}_c, p_m^{n+1} \rangle|. \tag{3.33}
\end{aligned}$$

Now, we estimate the last interface term in equation (3.33). Because  $\mathbf{u}_c^n$  and  $\mathbf{u}_c^{n+1}$  satisfy (3.2), by using (3.3) in Lemma 3.1, we obtain

$$\begin{aligned}
\Delta t |\langle (\mathbf{u}_c^n - \mathbf{u}_c^{n+1}) \cdot \mathbf{n}_c, p_m^{n+1} \rangle| &\leq C \Delta t \left\| \mathbf{u}_c^{n+1} - \mathbf{u}_c^n \right\| \left\| \nabla p_m^n \right\| \\
&\leq \frac{1}{6} \min\{\rho_1, \rho_2\} \left\| \mathbf{u}_c^{n+1} - \mathbf{u}_c^n \right\|^2 + \tilde{C} \Delta t^2 \left\| \nabla p_m^n \right\|^2. \tag{3.34}
\end{aligned}$$

By the triangle inequality, we have

$$\begin{aligned}
&-\frac{1}{2} \left[ \left\| \sigma^n (\tilde{\mathbf{u}}_c^{n+1} - \mathbf{u}_{c*}^n) \right\|^2 + \left\| \sigma^{n+1} (\mathbf{u}_c^{n+1} - \tilde{\mathbf{u}}_c^{n+1}) \right\|^2 + \left\| \sigma^n (\mathbf{u}_{c*}^n - \mathbf{u}_c^n) \right\|^2 \right] \\
&\leq -\frac{1}{6} \min\{\rho_1, \rho_2\} \left\| \mathbf{u}_c^{n+1} - \mathbf{u}_c^n \right\|^2. \tag{3.35}
\end{aligned}$$

Adding (3.33)–(3.35), we derive

$$\begin{aligned}
\mathcal{E}_{pd}^{n+1} - \mathcal{E}_{pd}^n &\leq -(\beta - \tilde{C}) \Delta t^2 \left\| \nabla p_m^{n+1} \right\|^2 - \Delta t \left\| \sqrt{2\nu^n} \mathbb{D} (\tilde{\mathbf{u}}_c^{n+1}) \right\|^2 - \frac{1}{4} \Delta t \left\| \sqrt{\mathbb{K}} \nabla (p_m^{n+1} - p_m^n) \right\|^2 \\
&\quad - \Delta t M_c \left\| \nabla w_c^{n+1} \right\|^2 - \Delta t M_m \left\| \nabla w_m^{n+1} \right\|^2 - \frac{\gamma\epsilon}{2} \left\| \nabla \phi_c^{n+1} - \nabla \phi_c^n \right\|^2 \\
&\quad - \frac{\gamma\epsilon}{2} \left\| \nabla \phi_m^{n+1} - \nabla \phi_m^n \right\|^2 - \frac{\gamma}{4\epsilon} \left\| R_c^{n+1} - R_c^n \right\|^2 - \frac{\gamma}{4\epsilon} \left\| R_m^{n+1} - R_m^n \right\|^2 \\
&\quad - \frac{S\gamma}{\epsilon} \left\| \phi_c^{n+1} - \phi_c^n \right\|^2 - \frac{S\gamma}{\epsilon} \left\| \phi_m^{n+1} - \phi_m^n \right\|^2 - \Delta t \frac{\alpha\sqrt{d}}{\sqrt{\text{trace}(\Pi)}} \langle \nu^n P_\tau \mathbf{u}_c^{n+1}, P_\tau \mathbf{u}_c^{n+1} \rangle. \tag{3.36}
\end{aligned}$$

If we impose  $\beta \geq 2\tilde{C}$  which only depends on the geometry of  $\Omega_m$  and  $\Omega_c$ , one can obtain (3.17). Thus, we complete the proof of Theorem 3.5.  $\square$

### 3.2. A fully decoupled scheme based on grad-div stabilized method

The time-stepping scheme (3.4)–(3.15) presented in the previous subsection decouples the Cahn–Hilliard–Navier–Stokes system in the free fluid region and the Cahn–Hilliard–Darcy system in the porous medium region. But the velocity and pressure in conduit are still coupled, while artificial boundary conditions is imposed to directly decouple the pressure and velocity resulting in the loss of accuracy [46]. In this subsection, we revise the partially decoupled scheme for a better efficiency. Specifically, we modify the standard pressure correction scheme in rotational version and introduce a grad-div stabilization [8, 9, 29, 36, 61] to completely decouple the velocity and pressure for Navier–Stokes equation while retaining the unconditionally stability stated as a discrete energy law.

In the first three steps of this new scheme, we follow the first three steps of the algorithm above to solve (3.4), (3.5), (3.7), (3.8), (3.9) sequentially for  $(\phi_m^{n+1}, w_m^{n+1})$ ,  $p_m^{n+1}$ , and  $(\phi_c^{n+1}, w_c^{n+1})$ , respectively. Then we solve the following decoupled systems to obtain  $\mathbf{u}_c^{n+1} \in \mathbf{X}_c$  and  $p_c^{n+1} \in Q_c$ .

**Step 4.** Find  $\mathbf{u}_c^{n+1} \in \mathbf{X}_c$ , such that

$$\begin{aligned} & \left( \rho^n \frac{\mathbf{u}_c^{n+1} - \mathbf{u}_c^n}{\Delta t}, \mathbf{v} \right) + (\rho^n (\mathbf{u}_c^n \cdot \nabla) \mathbf{u}_c^{n+1}, \mathbf{v}) + (2\nu^n \mathbb{D}(\mathbf{u}_c^{n+1}), \mathbb{D}(\mathbf{v})) - (w_c^{n+1} \nabla \phi_c^n, \mathbf{v}) \\ & + \frac{1}{2} \left( \mathbf{u}_c^{n+1} \frac{\rho^{n+1} - \rho^n}{\Delta t}, \mathbf{v} \right) - (p_c^n + s^n - s^{n-1}, \nabla \cdot \mathbf{v}) + \frac{1}{2} (\nabla \cdot (\rho^n \mathbf{u}_c^n) \mathbf{u}_c^{n+1}, \mathbf{v}) \\ & + \frac{\xi}{\Delta t} (\nabla \cdot (\mathbf{u}_c^{n+1} - \mathbf{u}_c^n), \nabla \cdot \mathbf{v}) + \langle p_m^{n+1}, \mathbf{v} \cdot \mathbf{n}_c \rangle - \frac{1}{2} \langle \rho^n \mathbf{u}_c^n \cdot \mathbf{u}_c^{n+1}, \mathbf{v} \cdot \mathbf{n}_c \rangle \\ & + \frac{\alpha \sqrt{d}}{\sqrt{\text{trace}(\Pi)}} \langle \nu^n P_\tau \mathbf{u}_c^{n+1}, P_\tau \mathbf{v} \rangle = 0, \end{aligned} \quad \forall \mathbf{v} \in \mathbf{X}_c. \quad (3.37)$$

**Step 5.** Find  $s^{n+1} \in Q_c$ , such that

$$(s^{n+1} - s^n, z) = -\frac{\zeta}{\Delta t} (\nabla \cdot \mathbf{u}_c^{n+1}, z), \quad \forall z \in Q_c, \quad (3.38)$$

where  $\zeta = \frac{1}{2} \min\{\rho_1, \rho_2\}$ .

**Step 6.** Find  $r^{n+1} \in Q_c$ , such that

$$(r^{n+1} - r^n, q) = -(\nabla \cdot \mathbf{u}_c^{n+1}, q), \quad \forall q \in Q_c. \quad (3.39)$$

**Step 7.** Compute  $p_c^{n+1} \in Q_c$  by

$$p_c^{n+1} = s^{n+1} + \hat{\nu} r^{n+1}, \quad (3.40)$$

where  $\hat{\nu} = \min\{\nu_1, \nu_2\}$ .

**Step 8.** Find  $R_c^{n+1} \in Y_c$  and  $R_m^{n+1} \in Y_m$ , such that

$$\left( \frac{R_c^{n+1} - R_c^n}{\Delta t}, \chi \right) = 2 \left( \phi_c^n \frac{\phi_c^{n+1} - \phi_c^n}{\Delta t}, \chi \right), \quad \forall \chi \in Y_c, \quad (3.41)$$

$$\left( \frac{R_m^{n+1} - R_m^n}{\Delta t}, \chi \right) = 2 \left( \phi_m^n \frac{\phi_m^{n+1} - \phi_m^n}{\Delta t}, \chi \right), \quad \forall \chi \in Y_m. \quad (3.42)$$

**Theorem 3.6.** Assume that stabilized parameter  $\beta$  is chosen to be large enough and  $\xi \geq \frac{3}{4} \min\{\rho_1, \rho_2\}$ . Then  $(\mathbf{u}_c^{n+1}, p_m^{n+1}, p_c^{n+1}, \phi_m^{n+1}, \phi_c^{n+1}, R_m^{n+1}, R_c^{n+1}, s^{n+1}, r^{n+1})$  defined by the fully decoupled time discretization (3.4)–(3.10) and (3.37)–(3.42) satisfies the following discrete energy law:

$$\mathcal{E}_{fd}^{n+1} - \mathcal{E}_{fd}^n \leq -\mathcal{D}_{fd}^{n+1}, \quad (3.43)$$

where  $\mathcal{E}_{fd}^n$  is defined as

$$\begin{aligned} \mathcal{E}_{fd}^n &= \frac{1}{2} \|\sigma^n \mathbf{u}_c^n\|^2 + \gamma \left[ \frac{\epsilon}{2} \|\nabla \phi_c^n\|^2 + \frac{1}{4\epsilon} \|R_c^n\|^2 \right] + \gamma \left[ \frac{\epsilon}{2} \|\nabla \phi_m^n\|^2 + \frac{1}{4\epsilon} \|R_m^n\|^2 \right] \\ &+ \frac{\xi}{2} \|\nabla \cdot \mathbf{u}_c^n\|^2 + \frac{1}{2} \Delta t \left\| \sqrt{\mathbb{K}} \nabla p_m^n \right\|^2 + \frac{1}{2} \hat{\nu} \Delta t \|r^n\|^2 + \frac{\Delta t^2}{2\zeta} \|s^n\|^2. \end{aligned} \quad (3.44)$$

and

$$\begin{aligned} \mathcal{D}_{fd}^{n+1} &= \frac{1}{4} \Delta t \left\| \sqrt{\mathbb{K}} \nabla (p_m^{n+1} - p_m^n) \right\|^2 + \Delta t M_c \|\nabla w_c^{n+1}\|^2 + \Delta t M_m \|\nabla w_m^{n+1}\|^2 + \frac{\gamma \epsilon}{2} \|\nabla \phi_c^{n+1} - \nabla \phi_c^n\|^2 \\ &+ \frac{\gamma \epsilon}{2} \|\nabla \phi_m^{n+1} - \nabla \phi_m^n\|^2 + \frac{\Delta t^2}{2\zeta} \|s^n - s^{n-1}\|^2 + \frac{\gamma}{4\epsilon} \|R_c^{n+1} - R_c^n\|^2 + \frac{\gamma}{4\epsilon} \|R_m^{n+1} - R_m^n\|^2 \\ &+ \frac{S\gamma}{\epsilon} \|\phi_c^{n+1} - \phi_c^n\|^2 + \frac{S\gamma}{\epsilon} \|\phi_m^{n+1} - \phi_m^n\|^2 + \Delta t \frac{\alpha \sqrt{d}}{\sqrt{\text{trace}(\Pi)}} \langle \nu^n P_\tau \mathbf{u}_c^{n+1}, P_\tau \mathbf{u}_c^{n+1} \rangle. \end{aligned}$$

*Proof.* We focus on discussion of the decoupling method for Navier–Stokes equation in conduit part.

By taking the test function  $\mathbf{v} = \Delta t \mathbf{u}_c^{n+1}$  in (3.37), combining with (3.20), and the identity (3.21), we obtain

$$\begin{aligned} & \frac{1}{2} \left[ \|\sigma^{n+1} \mathbf{u}_c^{n+1}\|^2 - \|\sigma^n \mathbf{u}_{c*}^n\|^2 + \|\sigma^n (\mathbf{u}_c^{n+1} - \mathbf{u}_{c*}^n)\|^2 \right] + \Delta t \left\| \sqrt{2\nu^n} \mathbb{D}(\mathbf{u}_c^{n+1}) \right\|^2 \\ & + \frac{\xi}{2} \left[ \|\nabla \cdot \mathbf{u}_c^{n+1}\|^2 - \|\nabla \cdot \mathbf{u}_c^n\|^2 + \|\nabla \cdot (\mathbf{u}_c^{n+1} - \mathbf{u}_c^n)\|^2 \right] \\ & - \Delta t (p_c^n + s^n - s^{n-1}, \nabla \cdot \mathbf{u}_c^{n+1}) + \Delta t \langle \mathbf{u}_c^{n+1} \cdot \mathbf{n}_c, p_m^{n+1} \rangle \\ & + \Delta t \frac{\alpha \sqrt{d}}{\sqrt{\text{trace}(\Pi)}} \langle \nu^n P_\tau \mathbf{u}_c^{n+1}, P_\tau \mathbf{u}_c^{n+1} \rangle = 0. \end{aligned} \quad (3.45)$$

Taking  $q = \hat{\nu} \Delta t r^n$  in (3.39) and taking the  $L_2$  inner product of (3.40) by  $q = \Delta t \nabla \cdot \mathbf{u}_c^{n+1}$  at time  $t^n$ , then adding these two equations, using the identity (3.21), we have

$$\frac{1}{2} \hat{\nu} \Delta t \left[ \|r^{n+1}\|^2 - \|r^n\|^2 - \|r^{n+1} - r^n\|^2 \right] + \Delta t (p_c^n, \nabla \cdot \mathbf{u}_c^{n+1}) - \Delta t (s^n, \nabla \cdot \mathbf{u}_c^{n+1}) = 0. \quad (3.46)$$

Summing up (3.45), (3.46), and (3.24), we obtain

$$\begin{aligned} & \frac{1}{2} \left[ \|\sigma^{n+1} \mathbf{u}_c^{n+1}\|^2 - \|\sigma^n \mathbf{u}_c^n\|^2 + \|\sigma^n (\mathbf{u}_c^{n+1} - \mathbf{u}_{c*}^n)\|^2 + \|\sigma^n (\mathbf{u}_{c*}^n - \mathbf{u}_c^n)\|^2 \right] + \Delta t \left\| \sqrt{2\nu^n} \mathbb{D}(\mathbf{u}_c^{n+1}) \right\|^2 \\ & + \frac{\xi}{2} \left[ \|\nabla \cdot \mathbf{u}_c^{n+1}\|^2 - \|\nabla \cdot \mathbf{u}_c^n\|^2 + \|\nabla \cdot (\mathbf{u}_c^{n+1} - \mathbf{u}_c^n)\|^2 \right] + \Delta t \langle \mathbf{u}_c^{n+1} \cdot \mathbf{n}_c, p_m^{n+1} \rangle \\ & + \frac{1}{2} \hat{\nu} \Delta t \left[ \|r^{n+1}\|^2 - \|r^n\|^2 - \|r^{n+1} - r^n\|^2 \right] + \Delta t \frac{\alpha \sqrt{d}}{\sqrt{\text{trace}(\Pi)}} \langle \nu^n P_\tau \mathbf{u}_c^{n+1}, P_\tau \mathbf{u}_c^{n+1} \rangle \\ & - \Delta t (2s^n - s^{n-1}, \nabla \cdot \mathbf{u}_c^{n+1}) = \Delta t (w_c^{n+1} \nabla \phi_c^n, \mathbf{u}_{c*}^n). \end{aligned} \quad (3.47)$$

Now, we estimate the term  $(2s^n - s^{n-1}, \nabla \cdot \mathbf{u}_c^{n+1})$ . Taking  $z = \frac{\Delta t^2}{\zeta} s^{n+1}$  in (3.38) and using (3.21), we obtain

$$\frac{\Delta t^2}{2\zeta} \left[ \|s^{n+1}\|^2 - \|s^n\|^2 + \|s^{n+1} - s^n\|^2 \right] = -\Delta t (\nabla \cdot \mathbf{u}_c^{n+1}, s^{n+1}). \quad (3.48)$$

Taking  $z = -\frac{\Delta t^2}{\zeta} (s^{n+1} - 2s^n + s^{n-1})$  in (3.38) and using (3.21), we obtain

$$-\frac{\Delta t^2}{2\zeta} \left[ \|s^{n+1} - s^n\|^2 - \|s^n - s^{n-1}\|^2 + \|s^{n+1} - 2s^n + s^{n-1}\|^2 \right] = \Delta t (\nabla \cdot \mathbf{u}_c^{n+1}, s^{n+1} - 2s^n + s^{n-1}). \quad (3.49)$$

On one hand, set  $z = \frac{\Delta t^2}{2\zeta} (s^{n+1} - 2s^n + s^{n-1})$  and taking the difference of (3.38) at step  $t^n$  and step  $t^{n+1}$  to derive

$$\frac{\Delta t^2}{2\zeta} \|s^{n+1} - 2s^n + s^{n-1}\|^2 \leq \frac{\zeta}{2} \|\nabla \cdot (\mathbf{u}_c^{n+1} - \mathbf{u}_c^n)\|^2. \quad (3.50)$$

On the other hand, set  $q = \frac{1}{2} \hat{\nu} \Delta t (r^{n+1} - r^n)$  in (3.39) to conclude that

$$\frac{1}{2} \hat{\nu} \Delta t \|r^{n+1} - r^n\|^2 \leq \frac{1}{2} \hat{\nu} \Delta t \|\nabla \cdot \mathbf{u}_c^{n+1}\|^2 \leq \frac{1}{4} \Delta t \left\| \sqrt{2\nu^n} \nabla \cdot \mathbf{u}_c^{n+1} \right\|^2 \leq \frac{1}{4} d \Delta t \left\| \sqrt{2\nu^n} \mathbb{D}(\mathbf{u}_c^{n+1}) \right\|^2. \quad (3.51)$$

where well-known Korn's inequality  $\|\nabla \cdot \mathbf{u}_c^{n+1}\|^2 \leq d \|\mathbb{D}(\mathbf{u}_c^{n+1})\|^2$  is used.

We add equations (3.47)–(3.51) to get

$$\frac{1}{2} \left[ \|\sigma^{n+1} \mathbf{u}_c^{n+1}\|^2 - \|\sigma^n \mathbf{u}_c^n\|^2 + \|\sigma^n (\mathbf{u}_c^{n+1} - \mathbf{u}_{c*}^n)\|^2 + \|\sigma^n (\mathbf{u}_{c*}^n - \mathbf{u}_c^n)\|^2 \right]$$



$$\begin{aligned}
& + \frac{\xi}{2} \left[ \|\nabla \cdot \mathbf{u}_c^{n+1}\|^2 - \|\nabla \cdot \mathbf{u}_c^n\|^2 + \|\nabla \cdot (\mathbf{u}_c^{n+1} - \mathbf{u}_c^n)\|^2 \right] + \frac{1}{2} \hat{\nu} \Delta t \left[ \|r^{n+1}\|^2 - \|r^n\|^2 \right] \\
& + \frac{\Delta t^2}{2\zeta} \left[ \|s^{n+1}\|^2 - \|s^n\|^2 + \|s^n - s^{n-1}\|^2 \right] + \Delta t \frac{\alpha \sqrt{d}}{\sqrt{\text{trace}(\Pi)}} \langle \nu^n P_\tau \mathbf{u}_c^{n+1}, P_\tau \mathbf{u}_c^{n+1} \rangle \\
& + \Delta t \langle \mathbf{u}_c^{n+1} \cdot \mathbf{n}_c, p_m^{n+1} \rangle \leq \frac{\zeta}{2} \|\nabla \cdot (\mathbf{u}_c^{n+1} - \mathbf{u}_c^n)\|^2 + \Delta t (w_c^{n+1} \nabla \phi_c^n, \mathbf{u}_{c*}^n). \tag{3.52}
\end{aligned}$$

Following the process in the proof of Theorem 3.5, one can derive (3.25) and (3.26) for CH equation in free flow region, and (3.32) for CHD system. Summing up (3.52), (3.25), (3.26) and (3.32), and applying Lemma 2.2, we have

$$\begin{aligned}
& \mathcal{E}_{fd}^{n+1} - \mathcal{E}_{fd}^n + \frac{1}{2} \left[ \|\sigma^{n+1}(\mathbf{u}_c^{n+1} - \mathbf{u}_{c*}^n)\|^2 + \|\sigma^n(\mathbf{u}_{c*}^n - \mathbf{u}_c^n)\|^2 \right] + \frac{1}{4} \Delta t \left\| \sqrt{\mathbb{K}} \nabla (p_m^{n+1} - p_m^n) \right\|^2 \\
& + \frac{\gamma\epsilon}{2} \|\nabla \phi_c^{n+1} - \nabla \phi_c^n\|^2 + \frac{\gamma\epsilon}{2} \|\nabla \phi_m^{n+1} - \nabla \phi_m^n\|^2 + \frac{\gamma}{4\epsilon} \|R_c^{n+1} - R_c^n\|^2 + \frac{\gamma}{4\epsilon} \|R_m^{n+1} - R_m^n\|^2 \\
& + \Delta t M_c \|\nabla w_c^{n+1}\|^2 + \Delta t M_m \|\nabla w_m^{n+1}\|^2 + \frac{S\gamma}{\epsilon} \|\phi_c^{n+1} - \phi_c^n\|^2 + \frac{S\gamma}{\epsilon} \|\phi_m^{n+1} - \phi_m^n\|^2 \\
& + \frac{\Delta t^2}{2\zeta} \|s^n - s^{n-1}\|^2 + \frac{\xi - \zeta}{2} \|\nabla \cdot (\mathbf{u}_c^{n+1} - \mathbf{u}_c^n)\|^2 + \Delta t \frac{\alpha \sqrt{d}}{\sqrt{\text{trace}(\Pi)}} \langle \nu^n P_\tau \mathbf{u}_c^{n+1}, P_\tau \mathbf{u}_c^{n+1} \rangle \\
& \leq -\beta \Delta t^2 \|\nabla p_m^{n+1}\|^2 + \Delta t |\langle (\mathbf{u}_c^n - \mathbf{u}_c^{n+1}) \cdot \mathbf{n}_c, p_m^{n+1} \rangle|. \tag{3.53}
\end{aligned}$$

Now, we estimate the last interface term in the above equation (3.53). We obtain by using (3.1)

$$\begin{aligned}
\Delta t |\langle (\mathbf{u}_{ch}^n - \mathbf{u}_{ch}^{n+1}) \cdot \mathbf{n}_c, p_m^{n+1} \rangle| & \leq C \Delta t \|\mathbf{u}_c^n - \mathbf{u}_c^{n+1}\|_{\mathbf{X}_{\text{div}}} \|\nabla p_m^n\| \\
& \leq \frac{1}{4} \min\{\rho_1, \rho_2\} \|\mathbf{u}_c^n - \mathbf{u}_c^{n+1}\|_{\mathbf{X}_{\text{div}}}^2 + \tilde{C} \Delta t^2 \|\nabla p_m^n\|^2 \\
& \leq \frac{1}{4} \|\sigma^n(\mathbf{u}_c^{n+1} - \mathbf{u}_c^n)\|^2 + \frac{1}{4} \min\{\rho_1, \rho_2\} \|\nabla \cdot (\mathbf{u}_c^n - \mathbf{u}_c^{n+1})\|^2 + \tilde{C} \Delta t^2 \|\nabla p_m^{n+1}\|^2. \tag{3.54}
\end{aligned}$$

We take the together with (3.53), (3.54) and (3.35) to obtain

$$\mathcal{E}_{fd}^{n+1} - \mathcal{E}_{fd}^n \leq -\mathcal{D}_{fd}^{n+1} - \left( \beta - \tilde{C} \right) \Delta t^2 \|\nabla p_m^{n+1}\|^2 - \frac{\xi - \zeta - \frac{1}{4} \min\{\rho_1, \rho_2\}}{2} \|\nabla \cdot (\mathbf{u}_c^{n+1} - \mathbf{u}_c^n)\|^2. \tag{3.55}$$

If we impose  $\beta \geq 2\tilde{C}$  and  $\xi \geq \frac{3}{4} \min\{\rho_1, \rho_2\}$ , we have (3.43). Therefore, we complete the proof of Theorem 3.6.  $\square$

#### 4. FULLY DISCRETE NUMERICAL SCHEMES

In this section, we present a fully discrete scheme by further discretizing the underlying spaces in the fully decouple time stepping scheme described by (3.4)–(3.10) and (3.37)–(3.42). Specifically, we let  $\mathfrak{X}_h$  be a quasi-uniform triangulation of domain  $\Omega$ , on which, we introduce finite element spaces  $Y_{jh}$ ,  $\mathbf{X}_{ch}$  and  $Q_{jh}$  with  $j = c, m$ . Here we further assume the finite element spaces  $\mathbf{X}_{ch}$  and  $Q_{ch}$  satisfy an inf-sup condition for the divergence operator in the following form: There exists a constant  $C > 0$  independent of  $h$  such that the LBB condition

$$\inf_{0 \neq q_h} \sup_{0 \neq \mathbf{v}_h} \frac{(\nabla \cdot \mathbf{v}_h, q_h)}{\|\mathbf{v}_h\|_1} \geq C \|q_h\|, \quad \forall q_h \in Q_{ch}, \mathbf{v}_h \in \mathbf{X}_{ch}$$

holds. Then, a fully discrete finite element method based on (3.4)–(3.10) and (3.37)–(3.42) is constructed as follows:

**Step 1.** Find  $(\phi_{mh}^{n+1}, w_{mh}^{n+1}) \in Y_{mh} \times Y_{mh}$ , such that

$$\begin{aligned} & \left( \frac{\phi_{mh}^{n+1} - \phi_{mh}^n}{\Delta t}, \psi_h \right) - (\mathbb{K} \nabla p_{mh}^n \cdot \nabla \phi_{mh}^n, \psi_h) + (\mathbb{K} w_{mh}^{n+1} \nabla \phi_{mh}^n \cdot \nabla \phi_{mh}^n, \psi_h) \\ & + (M_m \nabla w_{mh}^{n+1}, \nabla \psi_h) + \langle M_c \nabla w_{ch}^n \cdot \mathbf{n}_c, \psi_h \rangle + \langle \phi_{mh}^n - \phi_{ch}^n, \psi_h \rangle = 0, \quad \forall \psi_h \in Y_{mh}, \end{aligned} \quad (4.1)$$

$$\begin{aligned} & (w_{mh}^{n+1}, \omega_h) - \gamma \epsilon (\nabla \phi_{mh}^{n+1}, \nabla \omega_h) - \frac{\gamma}{\epsilon} (R_{mh}^n \phi_{mh}^n, \omega_h) - \frac{S\gamma}{\epsilon} (\phi_{mh}^{n+1} - \phi_{mh}^n, \omega_h) \\ & - \gamma \epsilon \langle \nabla \phi_{ch}^n \cdot \mathbf{n}_c, \omega_h \rangle + \langle w_{mh}^n - w_{ch}^n, \omega_h \rangle = 0, \quad \forall \omega_h \in Y_{mh}. \end{aligned} \quad (4.2)$$

**Step 2.** Find  $p_{mh}^{n+1} \in Q_{mh}$ , such that

$$(\mathbb{K} \nabla p_{mh}^{n+1}, \nabla q_h) - (\mathbb{K} w_{mh}^{n+1} \nabla \phi_{mh}^n, \nabla q_h) - \langle \mathbf{u}_{ch}^n \cdot \mathbf{n}_c, q_h \rangle + \beta \Delta t (\nabla p_{mh}^{n+1}, \nabla q_h) = 0, \quad \forall q_h \in Q_{mh}. \quad (4.3)$$

**Step 3.** Find  $(\phi_{ch}^{n+1}, w_{ch}^{n+1}) \in Y_{ch} \times Y_{ch}$ , such that

$$\begin{aligned} & \left( \frac{\phi_{ch}^{n+1} - \phi_{ch}^n}{\Delta t}, \psi_h \right) + \left( \left( \mathbf{u}_{ch}^n + \frac{1}{\rho^n} \Delta t w_{ch}^{n+1} \nabla \phi_{ch}^n \right) \cdot \nabla \phi_{ch}^n, \psi_h \right) + (M_c \nabla w_{ch}^{n+1}, \nabla \psi_h) \\ & + \langle M_m \nabla w_{mh}^{n+1} \cdot \mathbf{n}_m, \psi_h \rangle + \langle \phi_{ch}^{n+1} - \phi_{mh}^{n+1}, \psi_h \rangle = 0, \quad \forall \psi_h \in Y_{ch}, \end{aligned} \quad (4.4)$$

$$\begin{aligned} & (w_{ch}^{n+1}, \omega_h) - \gamma \epsilon (\nabla \phi_{ch}^{n+1}, \nabla \omega_h) - \frac{\gamma}{\epsilon} (R_{ch}^n \phi_{ch}^n, \omega_h) - \frac{S\gamma}{\epsilon} (\phi_{ch}^{n+1} - \phi_{ch}^n, \omega_h) \\ & - \gamma \epsilon \langle \nabla \phi_{mh}^n \cdot \mathbf{n}_m, \omega_h \rangle + \langle w_{ch}^{n+1} - w_{mh}^{n+1}, \omega_h \rangle = 0, \quad \forall \omega_h \in Y_{ch}. \end{aligned} \quad (4.5)$$

**Step 4.** Find  $\mathbf{u}_{ch}^{n+1} \in \mathbf{X}_{ch}$ , such that

$$\begin{aligned} & \left( \rho^n \frac{\mathbf{u}_{ch}^{n+1} - \mathbf{u}_{ch}^n}{\Delta t}, \mathbf{v}_h \right) + (\rho^n (\mathbf{u}_{ch}^n \cdot \nabla) \mathbf{u}_{ch}^{n+1}, \mathbf{v}_h) + (2\nu^n \mathbb{D}(\mathbf{u}_{ch}^{n+1}), \mathbb{D}(\mathbf{v}_h)) - (w_{ch}^{n+1} \nabla \phi_{ch}^n, \mathbf{v}_h) \\ & - (p_{ch}^n + s_h^n - s_h^{n-1}, \nabla \cdot \mathbf{v}_h) + \frac{1}{2} \left( \mathbf{u}_{ch}^{n+1} \frac{\rho^{n+1} - \rho^n}{\Delta t}, \mathbf{v}_h \right) + \frac{1}{2} (\nabla \cdot (\rho^n \mathbf{u}_{ch}^n) \mathbf{u}_{ch}^{n+1}, \mathbf{v}_h) \\ & + \frac{\xi}{\Delta t} (\nabla \cdot (\mathbf{u}_{ch}^{n+1} - \mathbf{u}_{ch}^n), \nabla \cdot \mathbf{v}_h) + \langle p_{mh}^{n+1}, \mathbf{v}_h \cdot \mathbf{n}_c \rangle - \frac{1}{2} \langle \rho^n \mathbf{u}_{ch}^n \cdot \mathbf{u}_{ch}^{n+1}, \mathbf{v}_h \cdot \mathbf{n}_c \rangle \\ & + \frac{\alpha \sqrt{d}}{\sqrt{\text{trace}(\Pi)}} \langle \nu^n P_\tau \mathbf{u}_{ch}^{n+1}, P_\tau \mathbf{v}_h \rangle = 0, \quad \forall \mathbf{v}_h \in \mathbf{X}_{ch}. \end{aligned} \quad (4.6)$$

**Step 5.** Find  $s_h^{n+1} \in Q_{ch}$ , such that

$$(s_h^{n+1} - s_h^n, z_h) = -\frac{\zeta}{\Delta t} (\nabla \cdot \mathbf{u}_{ch}^{n+1}, z_h), \quad \forall z_h \in Q_{ch}, \quad (4.7)$$

where  $\zeta = \frac{1}{2} \min\{\rho_1, \rho_2\}$ .

**Step 6.** Find  $r_h^{n+1} \in Q_{ch}$ , such that

$$(r_h^{n+1} - r_h^n, q_h) = -(\nabla \cdot \mathbf{u}_{ch}^{n+1}, q_h), \quad \forall q_h \in Q_{ch}. \quad (4.8)$$

**Step 7.** Compute  $p_{ch}^{n+1} \in Q_{ch}$  by

$$p_{ch}^{n+1} = s_h^{n+1} + \hat{\nu} r_h^{n+1}, \quad (4.9)$$

where  $\hat{\nu} = \min\{\nu_1, \nu_2\}$ .

**Step 8.** Find  $R_{ch}^{n+1} \in Y_{ch}$  and  $R_{mh}^{n+1} \in Y_{mh}$  such that

$$\left( \frac{R_{ch}^{n+1} - R_{ch}^n}{\Delta t}, \chi_h \right) = 2 \left( \phi_{ch}^n \frac{\phi_{ch}^{n+1} - \phi_{ch}^n}{\Delta t}, \chi_h \right), \quad \forall \chi_h \in Y_{ch}, \quad (4.10)$$

$$\left( \frac{R_{mh}^{n+1} - R_{mh}^n}{\Delta t}, \chi_h \right) = 2 \left( \phi_{mh}^n \frac{\phi_{mh}^{n+1} - \phi_{mh}^n}{\Delta t}, \chi_h \right), \quad \forall \chi_h \in Y_{mh}. \quad (4.11)$$

**Remark 4.1.** Comparing the above totally decoupled numerical algorithm with the numerical scheme in [40], the major differences include that (1) our method solves two separate Cahn–Hilliard equations in free fluid flow and porous medium regions, respectively, while, in [40], the two Cahn–Hilliard equations are viewed as a single Cahn–Hilliard on the whole domain. Thus, the treatment of interface conditions associated with phase function are also different from those in [40]; (2) the strategy in dealing with the stiffness of nonlinear term  $F(\phi)$  is different from those in [40], namely, the IEQ method is utilized to linearize the nonlinear system in this paper while a stabilized semi-implicit strategy is exploited in [40]; (3) the rotational pressure projection and grad-div stabilization are utilized to break the coupling of velocity and pressure for Navier–Stokes equation, while the artificial compression method is employed to decouple the coupling in [40]. Therefore, the proposed scheme in this paper is fully decoupled and more efficient, while the one in [40] is partially decoupled.

## 5. NUMERICAL EXAMPLE

In this section, several numerical examples are presented to illustrate the properties of proposed CHNSD model and developed numerical methods, such as the order of convergence, discrete energy decay law, and the evolution of a droplet under the influence of discontinuous permeability field, curve interface and buoyancy forces. In all examples, we employ the  $\mathbf{P}_2$ – $P_1$  Taylor-Hood elements for the Navier–Stokes equation and quadratic elements for the Darcy equation. We also utilize the quadratic elements for Cahn–Hilliard equation in both subdomains, *i.e.*, free flow region and porous medium, respectively.

**Example 1** (Convergence and accuracy). Consider the CHNSD model problem without the inertial force on the interface on the computational domain  $\Omega = [0, 1] \times [0, 2]$ ,  $\Omega_m = [0, 1] \times [0, 1]$ ,  $\Omega_c = [0, 1] \times [1, 2]$ , and  $[0, T]$  with terminal time  $T = 5$ . Choose the parameters  $\nu_1 = 1$ ,  $\nu_2 = 1.1$ ,  $\rho_1 = 1$ ,  $\rho_2 = 3$ ,  $M_m = 1$ ,  $\gamma = 1$ ,  $\epsilon = 1$ ,  $M_c = 1$ ,  $\xi = 5$ ,  $S = 2$ ,  $\beta = 2$  and  $\mathbb{K} = \mathbb{I}$ . The source terms in the model are chosen such that the following functions are the solutions:

$$\begin{aligned} p_m &= \phi_m = w_m = g(x)g_m(y) \cos(\pi t), \\ \mathbf{u}_c &= \left[ x^2(y-1)^2 \cos(\pi t), -\frac{2}{3}x(y-1)^3 \cos(\pi t) \right]^T, \\ p_c &= \phi_c = w_c = g(x)g_c(y) \cos(\pi t), \end{aligned}$$

where  $g(x) = 16x^2(x-1)^2$ ,  $g_m(y) = 16y^2(y-1)^2$ ,  $g_c(y) = 16(y-1)^2(y-2)^2$ .

A uniform triangular mesh and a uniform time partition are used in this simulation. Numerical errors are listed in Table 1 for the approximations to velocity and phase variable and pressure in fluid flow generated by decoupled linearized numerical scheme at final time  $T = 5$  which is consistent with the expected optimal convergence of this scheme.

**Example 2** (Convergence for varying permeability). In order to validate the effects of proposed numerical method for CHNSD model with varying permeability parameters, we take  $\mathbb{T}(\mathbf{u}_c, p_c) = \nu \nabla \mathbf{u}_c - p_c \mathbb{I}$  and  $\mathbb{K} = k \mathbb{I}$ . The exact solution is given by [71]

$$p_m = \left( \frac{1}{k} \left( x(1-x)(y-1) + \frac{1}{3}y^3 - y^2 + y \right) + 2x \right) \cos(t),$$

TABLE 1. Numerical errors at  $T = 5$  and convergence rates of fully decoupled numerical method with  $\Delta t = 0.01h$ .

$1/h$	$\ p_{mh} - p_m\ _1$	Rate	$\ \phi_{mh} - \phi_m\ _1$	Rate	$\ \mathbf{u}_{ch} - \mathbf{u}_c\ _1$	Rate	$\ p_{ch} - p_c\ $	Rate	$\ \phi_{ch} - \phi_c\ _1$	Rate
8	9.4997E-2	—	1.2595E-1	—	7.0137E-3	—	4.9277E-2	—	1.2657E-1	—
16	2.3888E-2	1.99	3.7769E-2	1.74	2.1984E-3	1.67	1.1511E-2	2.10	3.7611E-2	1.75
32	6.0304E-3	1.99	1.0360E-2	1.87	6.0892E-4	1.85	3.1161E-3	1.89	1.0292E-2	1.87
64	1.5175E-3	1.99	2.7024E-3	1.94	1.5991E-4	1.93	8.3672E-4	1.90	2.6828E-3	1.94
128	3.8098E-4	1.99	6.8521E-4	1.98	4.0829E-5	1.97	2.1568E-4	1.96	6.8135E-4	1.98

TABLE 2. Numerical relative errors at  $T = 5$  and convergence rates of fully decoupled numerical method with  $k = 0.1$  and  $\Delta t = 0.01h$ .

$1/h$	$\ p_{mh} - p_m\ _1$	Rate	$\ \phi_{mh} - \phi_m\ _1$	Rate	$\ \mathbf{u}_{ch} - \mathbf{u}_c\ _1$	Rate	$\ p_{ch} - p_c\ $	Rate	$\ \phi_{ch} - \phi_c\ _1$	Rate
8	3.4443E-2	—	6.9022E-2	—	1.1073E-2	—	3.4389E-3	—	1.7953E-3	—
16	9.4343E-3	1.87	2.0806E-2	1.73	3.8093E-3	1.54	1.0155E-3	1.76	5.4223E-4	1.73
32	2.4548E-3	1.94	5.6746E-3	1.87	1.0895E-3	1.81	2.6813E-4	1.92	1.4795E-4	1.87
64	6.2673E-4	1.97	1.4804E-3	1.94	2.9264E-4	1.90	6.9618E-5	1.95	3.8604E-5	1.94
128	1.5672E-4	2.00	3.7568E-4	1.98	7.5672E-5	1.95	1.7606E-5	1.98	9.8054E-6	1.98

TABLE 3. Numerical relative errors at  $T = 5$  and convergence rates of fully decoupled numerical method with  $k = 0.01$  and  $\Delta t = 0.01h$ .

$1/h$	$\ p_{mh} - p_m\ _1$	Rate	$\ \phi_{mh} - \phi_m\ _1$	Rate	$\ \mathbf{u}_{ch} - \mathbf{u}_c\ _1$	Rate	$\ p_{ch} - p_c\ $	Rate	$\ \phi_{ch} - \phi_c\ _1$	Rate
8	3.2912E-2	—	6.9013E-2	—	4.5422E-2	—	2.9849E-3	—	1.7960E-3	—
16	8.6221E-3	1.93	2.0802E-2	1.73	1.5414E-2	1.56	8.5388E-4	1.81	5.4218E-4	1.73
32	2.1857E-3	1.98	5.6737E-3	1.87	4.3813E-3	1.81	2.1099E-4	2.02	1.4794E-4	1.87
64	5.5052E-4	1.99	1.4802E-3	1.94	1.1657E-3	1.91	5.3591E-5	1.98	3.8601E-5	1.94
128	1.3823E-4	1.99	3.7694E-4	1.97	3.0353E-4	1.94	1.3569E-5	1.98	9.8387E-6	1.97

$$\begin{aligned}
\phi_m &= w_m = g(x)g_m(y) \cos(t), \\
\mathbf{u}_c &= [(y^2 - 2y + 1) \cos(t), (x^2 - x) \cos(t)]^T, \\
p_c &= \left( 2\nu(x + y - 1) + \frac{1}{3k} \right) \cos(t), \\
\phi_c &= w_c = g(x)g_c(y) \cos(t),
\end{aligned}$$

where  $g(x)$ ,  $g_m(y)$  and  $g_c(y)$  are defined in Example 1. The initial conditions and the sourcing terms are chosen from this solution. The computational domain and parameters are taken as same as in Example 1 except  $k = 0.1$ ,  $k = 0.01$  and  $k = 0.001$ .

The orders of magnitude for  $p_c$  and  $p_m$  increase as  $k$  decreases, thus we report the relative errors instead of absolute errors. The relative errors is defined by  $|v_h^n - v(t_n)|/|v(t_n)|$  with respect to  $L^2$  norm  $\|\cdot\|$  and  $H^1$  norm  $\|\cdot\|_1$  for  $|\cdot|$  between approximate solution  $v_h^n$  and exact solution  $v(t_n)$ . Tables 2–4 exhibit the relative errors of numerical approximations at  $T = 5$  with uniformly refined mesh  $h = \frac{1}{8}, \frac{1}{16}, \frac{1}{32}, \frac{1}{64}, \frac{1}{128}$  corresponding to  $k = 0.1, 0.01, 0.001$ . From Tables 2 to 4, one can see that the error norms with respect to variables  $p_m$ ,  $\phi_m$ ,  $\mathbf{u}_c$ ,  $p_c$ , and  $\phi_c$  have the satisfied order of convergence when the hydraulic conductivity  $\mathbb{K}$  varies.

**Example 3** (Shape relaxation and energy dissipation). In this example, we simulate the evolution of a initial cross shape phase function in domain  $\Omega = [0, 2] \times [0, 1]$  with  $\Omega_c = [0, 1] \times [0, 1]$ ,  $\Omega_m = [1, 2] \times [0, 1]$ , in order to

TABLE 4. Numerical relative errors at  $T = 5$  and convergence rates of fully decoupled numerical method with  $k = 0.001$  and  $\Delta t = 0.005h$ .

$1/h$	$\ p_{mh} - p_m\ _1$	Rate	$\ \phi_{mh} - \phi_m\ _1$	Rate	$\ \mathbf{u}_{ch} - \mathbf{u}_c\ _1$	Rate	$\ p_{ch} - p_c\ $	Rate	$\ \phi_{ch} - \phi_c\ _1$	Rate
8	3.1854E-2	–	6.8971E-2	–	8.0329E-2	–	2.1749E-4	–	1.7954E-3	–
16	8.2001E-3	1.96	2.0795E-2	1.73	2.6697E-2	1.59	7.3593E-5	1.56	5.4205E-4	1.73
32	2.0548E-3	2.00	5.6729E-3	1.87	7.5638E-3	1.82	2.2554E-5	1.71	1.4793E-4	1.87
64	5.1474E-4	2.00	1.4801E-3	1.94	2.0301E-3	1.90	6.3718E-6	1.82	3.8601E-5	1.94
128	1.2885E-4	2.00	3.7696E-4	1.97	5.2568E-4	1.95	1.6136E-6	1.98	9.8701E-6	1.97

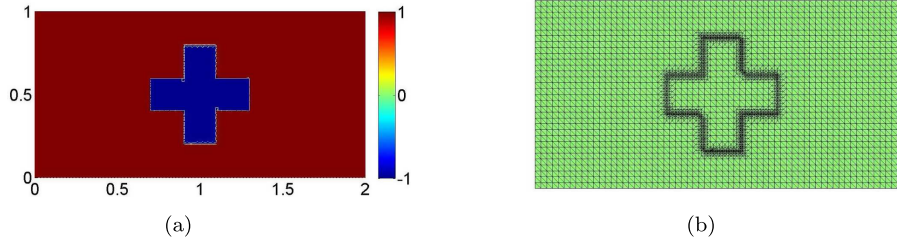


FIGURE 2. Contour plots of cross shape. (a) Initial phase function. (b) Initial adaptive mesh.

illustrate the shape relaxation based on the expected energy dissipation. Set parameters  $\gamma = 0.01$ ,  $\epsilon = 0.01$ ,  $\nu = 1$ ,  $M_c = 0.005$ ,  $M_m = 0.005$  and  $\mathbb{K} = 0.002\mathbb{I}$  and take the initial velocity and pressure to be zero. We run the simulation until  $T = 20$ .

In the rest of the simulations, we shall use a spatial mesh adaptive strategy from [52] to improve the accuracy for capturing the interface layer without increasing computational costs excessively. Specifically, based on the observations in [56], adaptive mesh strategy uses at least four grid elements across the transition interface between two-phase fluids. In our computations for the rest of the examples, the uniform fundamental mesh has a mesh size of  $h = \frac{1}{32}$  on which this mesh adaptive strategy related to the value of  $|\nabla\phi|$  is applied around the interface.

The initial shape and adaptive mesh of phase function are shown in a cross shape is depicted Figure 2. Figure 3 shows the dynamical morphotype of the simulated phase function from the initial cross shape relaxing to a circular shape under the effect of surface tension associated with the density ratio  $\rho_1 : \rho_2 = 1 : 5$  and uniform time partition  $\Delta t = 0.005$ , which is in a good agreement with the benchmark study in [2, 55]. The discrete mass and energy of numerical results are plotted in Figure 4. It is clear that the discrete mass is conserved and the discrete energy-decay property is observed. We would like to point out that an asymmetrical behavior of the morphotype on the two sides of the sharp interface between the porous media and the free flow region. This phenomenon shows that the relaxation in the free flow region is faster than that of the porous media region, due to the faster flow speed of the free flow.

The adaptive mesh and phase variable on enlarged adaptive grid are illustrated in Figure 5. As shown in this figure, the evolution of interface can be accurately captured under the adaptive strategy utilized in this paper. And the adaptive meshes are well concentrated near the interface region between the binary phase fluids at each time step.

**Example 4 (Merging drops).** In this section, the coalescence of four square droplets is simulated to investigate the effect of surface tension and unconditionally energy stability of proposed numerical method. Choose parameters  $\gamma = 0.01$ ,  $\epsilon = 0.01$ ,  $\nu = 1$ ,  $M_c = 0.005$ ,  $M_m = 0.005$ ,  $\mathbb{K} = 0.002\mathbb{I}$ ,  $\rho_1 : \rho_2 = 1 : 3$ , we set the initial velocity and pressure to be zero on coupled free flow region  $[0, 1] \times [0, 0.5]$  and porous medium  $[0, 1] \times [0.5, 1]$ .

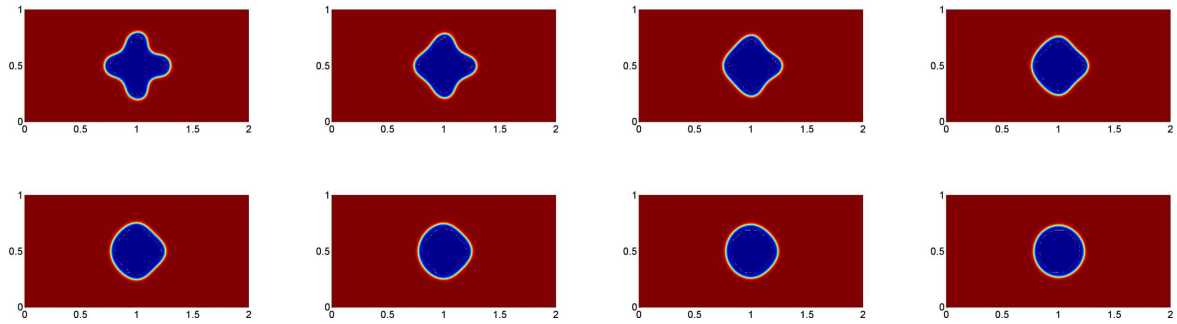


FIGURE 3. The dynamics of a cross shape bubble. All the sub-figures are indexed from left to right row by row as follows: (a)  $t = 2.0$ , (b)  $t = 4.0$ , (c)  $t = 6.0$ , (d)  $t = 8.0$ , (e)  $t = 10.0$ , (f)  $t = 12.0$ , (g)  $t = 15.0$ , (h)  $t = 20.0$ .

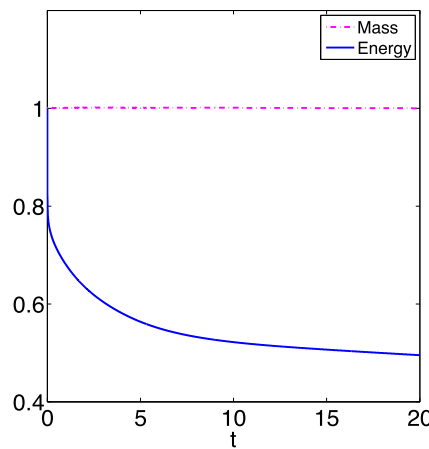


FIGURE 4. The evolution of discrete energy and mass conservation of cross shape.

The initial behavior of phase function  $\phi$  is characterized by four independent square droplets with width equal to 0.4. The terminal time is set to  $T = 40$ .

As expected from the literature for this type of benchmark study [99], Figure 6a displays the discrete energy and evolutions of phase variables under  $\Delta t = 0.005$ . This figure clearly shows that the four individual square droplets firstly evolve to four circle droplets, then start the coalescence, and finally merge into a single circle, which remains unchanged over time. The discrete energy of numerical algorithms is plotted in Figure 6b associated with different time step sizes. From Figure 6, the discrete energy-decay property is indeed satisfied and the discrete energy achieves the minimum value. This observation numerically verifies theoretical results of the unconditional stability of discrete energy. In fact, all the cases presented in Figure 6b relax the four separate square shapes to the circular shape. Since the procedure is similar to Figure 6a, we omit the detailed pictures here.

**Example 5** (Discontinuous permeability field). In this example, we simulate a droplet being pushed by the boundary-driven flow from the free flow region to the heterogeneous porous medium with discontinuous hydraulic conductivity tensor  $\mathbb{K} = k(x, y)\mathbb{I}$ . We take parameters  $M = 0.01$ ,  $\gamma = 0.01$ ,  $\epsilon = 0.01$ ,  $\nu = 1$ ,  $\rho_1 = 1$ ,  $\rho_2 = 5$ , and  $\Delta t = 0.001$  on computing domain  $\Omega = [0, 2] \times [0, 1]$  with  $\Omega_c = [0, 1] \times [0, 1]$ ,  $\Omega_m = [1, 2] \times [0, 1]$ . Imposing

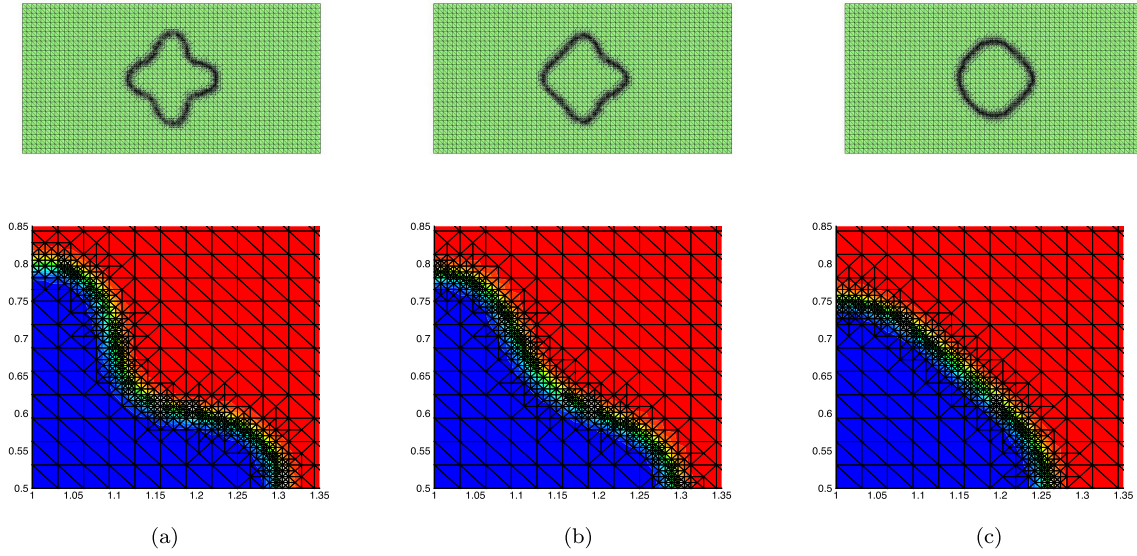


FIGURE 5. The adaptive mesh refinement and the enlarged adaptive mesh refinement. (a)  $t = 2.0$ . (b)  $t = 4.0$ . (c)  $t = 10.0$ .

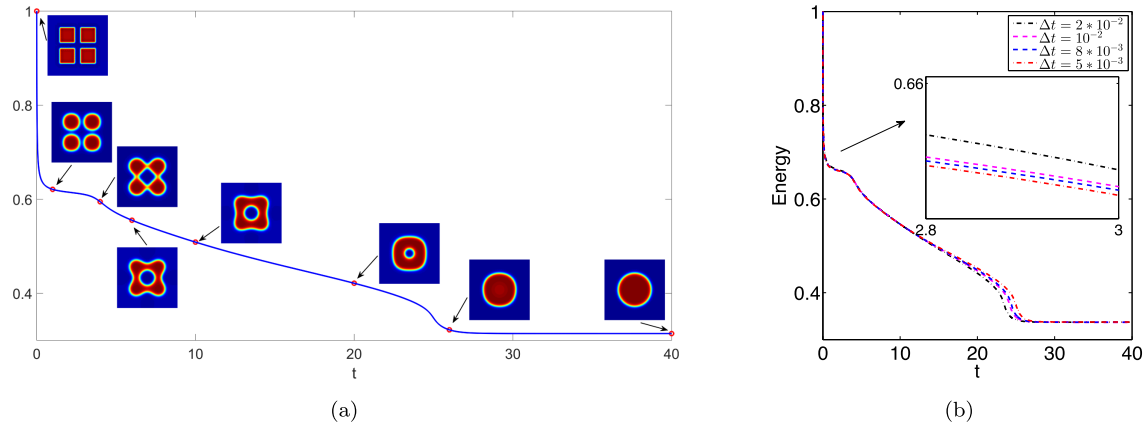


FIGURE 6. The evolution of discrete energy of merging drops. (a) Dynamic of phase variable. (b) Energy evolution.

the parabolic velocity  $\mathbf{u}_c = -4y(y-1)$  on the left boundary  $\Gamma_{in} := \{0\} \times [0, 1]$  and setting the pressure to be 0 on right boundary on  $\Gamma_{out} := \{2\} \times [0, 1]$ , the initial condition for the phase function is given by the following hyperbolic tangent function,

$$\phi_0 = -\tanh\left(\left(0.15 - \sqrt{(x-0.3)^2 + (y-0.5)^2}\right)/(\sqrt{2}\epsilon)\right). \quad (5.1)$$

In order to investigate the influence of hydraulic conductivity tensor, we consider three different cases for discontinuous permeability in porous medium shown in Figure 7 as follows:

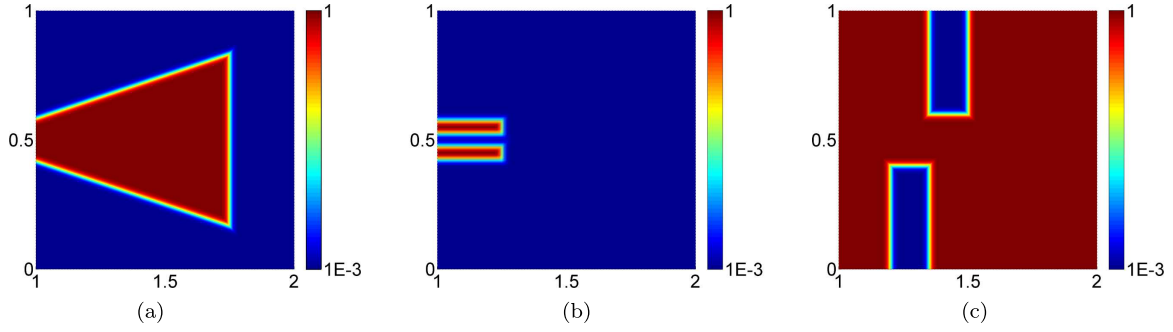


FIGURE 7. Discontinuous permeability field. (a) Trapezoid channel. (b) Two cracks. (c) Two rocks.

**Case I:** the permeability is depicted by

$$k(x, y) = 0.501 - 0.5 \tanh\left(\frac{\max(|x - 1.25| - 0.5, |y - 0.5| - x/3 + 0.25)}{\sqrt{2}\epsilon}\right), \quad (5.2)$$

where a trapezoid channel with intrinsic permeability equal to  $\mathbb{I}$  surrounded by a matrix with intrinsic permeability equal to  $10^{-3}\mathbb{I}$ ; four corner points are  $(x_i, 0.75 - x_i/3)$ ,  $(x_i, 0.25 + x_i/3)$  with  $x_1 = 1, x_2 = 1.75$ , see Figure 7a;

**Case II:** the permeability is depicted by

$$k(x, y) = 0.501 + 0.5 \left(1 - \sum_{i=1}^2 \tanh\left(\frac{\max(|x - x_i| - 0.125, |y - y_i| - 0.025)}{\sqrt{2}\epsilon}\right)\right), \quad (5.3)$$

where two horizontal cracks centered at  $(x_1, y_1) = (1.125, 0.55)$  and  $(x_2, y_2) = (1.125, 0.45)$ , respectively; their length and width equal to 0.25 and 0.05, respectively, see Figure 7b;

**Case III:** the permeability is depicted by

$$k(x, y) = 0.501 + 0.5 \left(-1 + \sum_{i=1}^2 \tanh\left(\frac{\max(|x - x_i| - 0.075, |y - y_i| - 0.2)}{\sqrt{2}\epsilon}\right)\right), \quad (5.4)$$

where two vertical rectangular rocks centered at  $(x_1, y_1) = (1.425, 0.8)$  and  $(x_2, y_2) = (1.275, 0.2)$ , respectively; their height and width equal to 0.4 and 0.15, respectively, see Figure 7c.

Figures 8–10 show the snapshots of interfaces between binary fluids from left to right across the interface  $x = 1$ . We clearly see that the mobile moves toward the center region with high hydraulic conductivity, for example at times  $t = 0.5$  and  $t = 0.6$  for Case I depicted in Figure 8, and deforms into a flatter shape at the front propagating in porous media. The mobile can seek pathways toward high permeability across the interface  $x = 1$  as expected due to the effect of hydraulic conductivity in porous media region for all three cases. After the deformed droplet smoothly goes across the interface  $x = 1$ , the droplet is further deformed in the porous media and then reached the steady shape.

Figure 11 shows the streamline and the contours of norm of velocity with the brighter color indicating higher speed of the flow. We observe that the velocity is larger inside the trapezoidal region of case I, inside the two horizontal cracks of case II, and outside the two vertical rocks of case III, respectively. The fluid flows toward the high permeability areas for all cases. The expected flow patterns are observed for different permeability values.



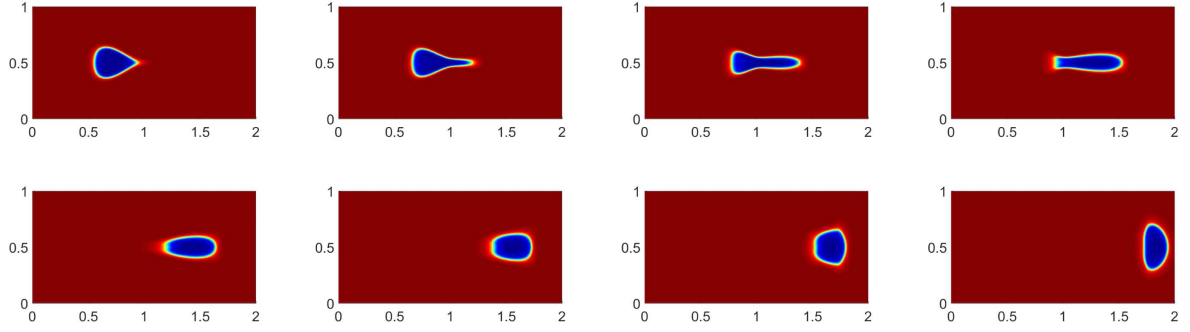


FIGURE 8. The evolution of droplet in a channel heterogeneous medium. All the subfigures are indexed from left to right row by row as follows:  $t = 0.4, 0.5, 0.6, 0.7, 0.8, 0.9, 1.0, 1.2$ .

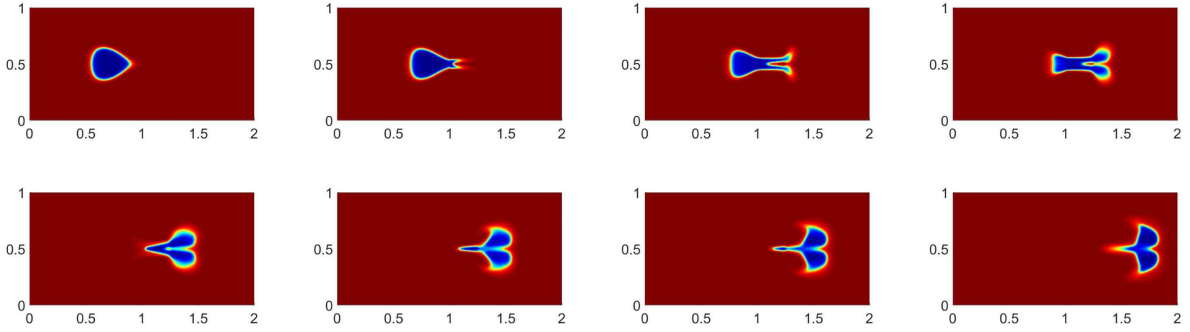


FIGURE 9. The evolution of droplet in porous medium with two cracks. All the subfigures are indexed from left to right row by row as follows:  $t = 0.4, 0.5, 0.6, 0.7, 0.8, 0.9, 1.0, 1.3$ .

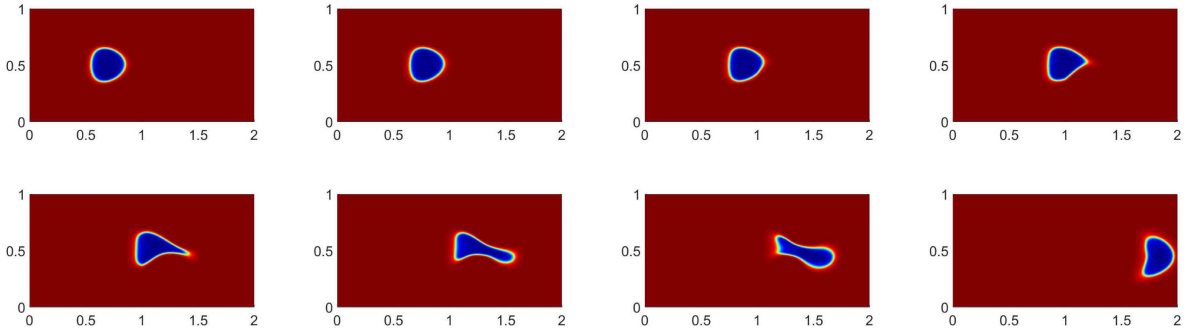


FIGURE 10. The evolution of droplet in porous medium with two rocks. All the subfigures are indexed from left to right row by row as follows:  $t = 0.4, 0.5, 0.6, 0.7, 0.8, 0.9, 1.0, 1.35$ .

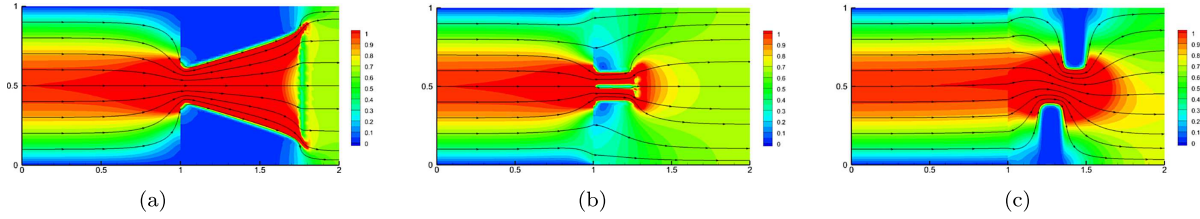


FIGURE 11. Velocity and streamlines at  $t = 0.5$  for Example 3. (a) Trapezoid channel. (b) Two cracks. (c) Two rocks.

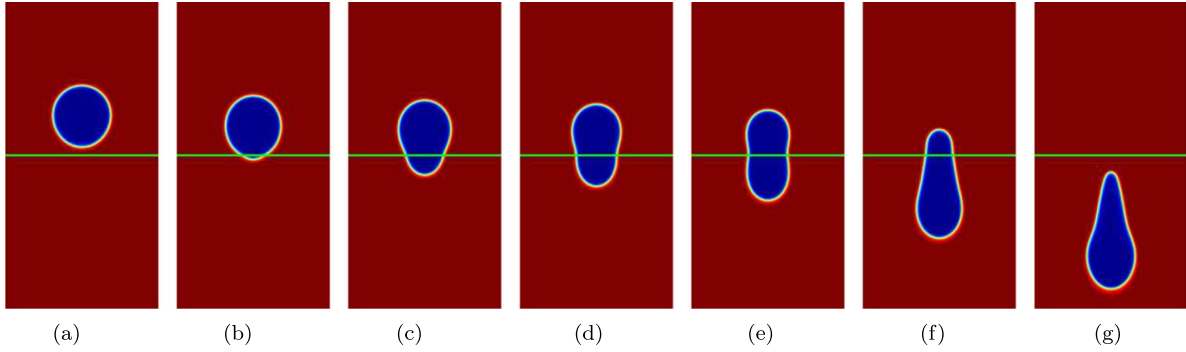


FIGURE 12. The deformation of droplet falling across the straight interface. (a)  $t = 2.0$ . (b)  $t = 4.0$ . (c)  $t = 4.5$ . (d)  $t = 4.75$ . (e)  $t = 5.0$ . (f)  $t = 5.5$ . (g)  $t = 6.0$ .

**Example 6** (Falling droplet under gravity force). In this section, the drop falling surrounded by a less dense medium is simulated and investigated in a vertical channel  $\Omega = [0, 1] \times [0, 2]$  composing of the porous media region  $\Omega_m = [0, 1] \times [1, 2]$  and free flow region  $\Omega_c = [0, 1] \times [0, 1]$ . The parameters are  $\gamma = 0.01$ ,  $\epsilon = 0.01$ ,  $\nu = 1$ ,  $M_c = 0.01$ ,  $M_m = 0.01$ ,  $\mathbb{K} = 0.1\mathbb{I}$ ,  $\rho_1 = 1$ , and  $\rho_2 = 10$ . The pressure is set to zero on the top boundary  $[0, 1] \times \{2\}$ . We take the following initial position for phase function

$$\phi_m^0(x, y) = \tanh\left(\left(0.2 - \sqrt{(x - 0.5)^2 + (y - 1.3)^2}\right) / (\sqrt{2}\epsilon)\right). \quad (5.5)$$

Figure 12 shows the dynamics of the droplet falling and turning into an ellipse in time under the effect of gravity force and surface tension. Here the green line indicates the interface between two subdomains. The droplet has a more pronounced deformation once it crosses the interface  $y = 1$  entering free flow region. We also consider the curve interface between two subregions. Figure 13 describes the process of the droplet falling across the curve interface. Comparing Figures 12 and 13, the interface morphology shows a significant effect on the droplet deformation, which implies the importance of interface between free flow region and porous medium to the evolution of droplet.

**Example 7** (Buoyancy-driven flow). In this experiment, we further validate the applicability of proposed numerical scheme by simulating a rising bubble in a heavier medium with respect to different density variations. The computational domain is chosen as  $\Omega = [0, 1] \times [0, 2]$  associated with the interface boundary  $\Gamma = [0, 1] \times \{1\}$  between the porous media region  $\Omega_m = [0, 1] \times [1, 2]$  and free flow region  $\Omega_c = [0, 1] \times [0, 1]$ . Choose  $\gamma = 0.01$ ,  $\epsilon = 0.01$ ,  $\nu = 1$ ,  $M_c = 0.01$ ,  $M_m = 1$ , and  $\mathbb{K} = 0.1\mathbb{I}$ . The initial location for phase function is taken as

$$\phi_c^0(x, y) = \tanh\left(\left(0.2 - \sqrt{(x - 0.5)^2 + (y - 0.5)^2}\right) / (\sqrt{2}\epsilon)\right). \quad (5.6)$$

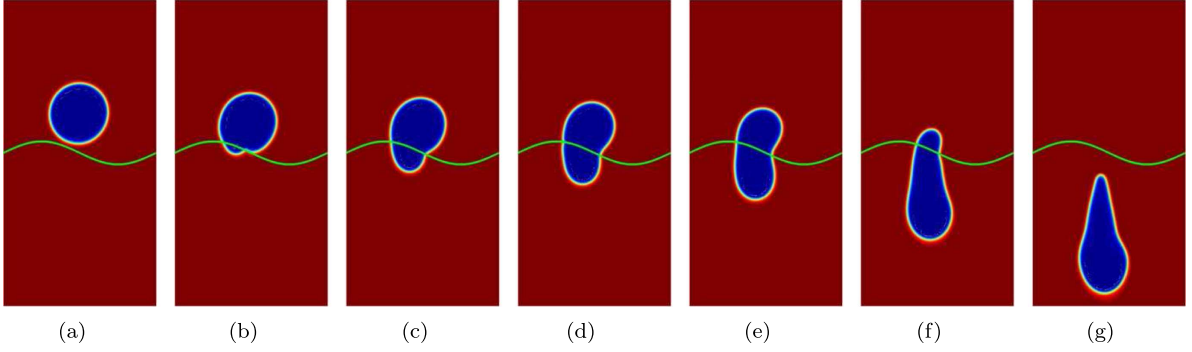


FIGURE 13. The deformation of droplet falling across the curve interface. (a)  $t = 2.0$ . (b)  $t = 4.0$ . (c)  $t = 4.5$ . (d)  $t = 4.75$ . (e)  $t = 5.0$ . (f)  $t = 5.5$ . (g)  $t = 6.0$ .

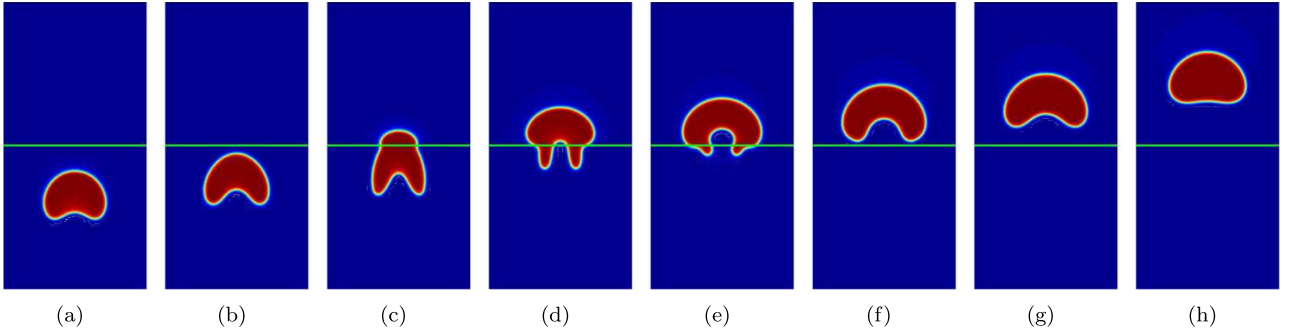


FIGURE 14. The evolution of a arising bubble. (a)  $t = 1.0$ . (b)  $t = 1.5$ . (c)  $t = 2.0$ . (d)  $t = 2.5$ . (e)  $t = 3.0$ . (f)  $t = 3.5$ . (g)  $t = 4.0$ . (h)  $t = 5.0$ .

Figure 14 shows the evolution of bubble from conduit to matrix across the interface for the density ratio  $\rho_1 : \rho_2 = 1 : 50$ , where  $\phi = 1$  (red color) represents the lighter fluid and  $\phi = -1$  (blue color) represents the heavier fluid. We can clearly observe the deformation of the bubble under the effect of surface tension, the sharp interface between the two subdomains, and the porous media. We can see that the numerical simulations are consistent with the results in [27].

Furthermore, evolutions of two coaxial bubbles [13, 85] are considered with the following initial condition

$$\phi_c^0(x, y) = 1 + \sum_{i=1}^2 \tanh\left(\left(0.15 - \sqrt{(x - x_i)^2 + (y - y_i)^2}\right) / \left(\sqrt{2}\epsilon\right)\right), \quad (5.7)$$

where  $(x_1, y_1) = (0.5, 0.25)$  and  $(x_2, y_2) = (0.5, 0.6)$ . The other parameters are same with the one bubble rising case. The dynamics of rising bubbles are recorded in Figure 15 which demonstrates the coalescence and ascension of two bubbles. It can be observed that the two merging droplets eventually evolve into the stable shape. Similar numerical behaviour was reported in [23]. The reasonable results further validate the numerical schemes.

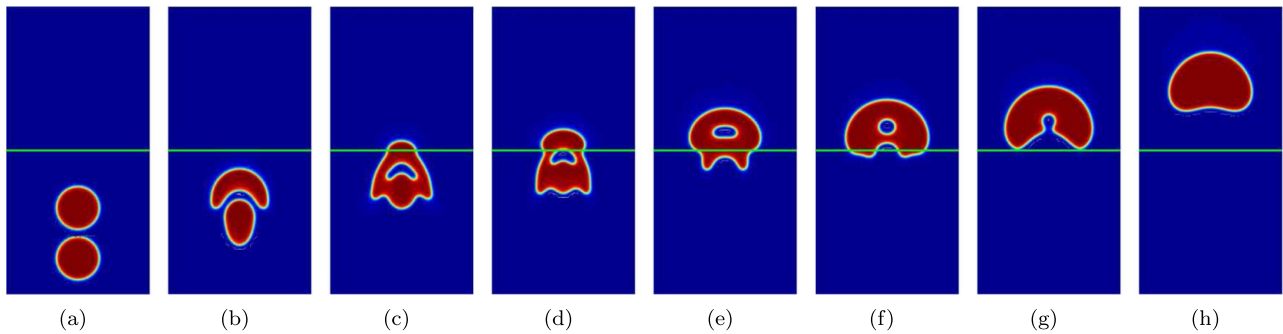


FIGURE 15. The evolution of vertical rising bubbles arising drop. (a)  $t = 0.0$ . (b)  $t = 1.0$ . (c)  $t = 1.75$ . (d)  $t = 2.0$ . (e)  $t = 2.5$ . (f)  $t = 3.0$ . (g)  $t = 3.5$ . (h)  $t = 5.0$ .

## 6. CONCLUSIONS

In this paper, a fully decoupled finite element scheme with discrete energy law is developed for two-phase flows with different densities and viscosities in the free fluid region and porous media region, which are coupled by suitable interface conditions. An energy law is derived for the novel weak formulation. The CHNS equation and CHD equation on the two different subdomains are decomposed base on the seven interface conditions. IEQ technique is utilized to deal with the stiffness of the phase function associated with the interfacial width in the phase function. The application of these ideas result in a CHNS equation and a CHD equation that can be resolved separately at each time step. We further decouple the CHNS equation into CH equation and Navier–Stokes equation in conduit and decouple the CHD equation into CH equation and Darcy equation in the matrix. Furthermore, the modified pressure correction and grad-div stabilization technique are utilized to deal with the difficulties arising from the decoupling of velocity and pressure in Navier–Stokes equation. At the end, the proposed fully-decoupled scheme only needs to solve a sequence of linear equations at each discrete time level. The full discretization is constructed in the framework of the finite element method. The discrete energy law is analyzed for the proposed method. The efficiency and unconditional stability of the proposed schemes are verified by numerical simulations. We have also investigated the dynamic behavior of challenging model scenarios to validate the mathematical model and numerical method.

*Acknowledgements.* This work is supported in part by the National Natural Science Foundation of China grants NSFC grant 11901461, China Postdoctoral Science Foundation 2020M673464, NSF grants DMS-1818642 and DMS-2152609, Hong Kong Special Administrative Region GRF grant 15302418.

## REFERENCES

- [1] H. Abels, H. Garcke and G. Grün, Thermodynamically consistent, frame indifferent diffuse interface models for incompressible two-phase flows with different densities. *Math. Models Methods Appl. Sci.* **22** (2012) 1150013.
- [2] P.F. Antonietti, L. Veiga, S. Scacchi and M. Verani, A  $C^1$  virtual element method for the Cahn–Hilliard equation with polygonal meshes. *SIAM J. Numer. Anal.* **54** (2016) 34–56.
- [3] T. Arbogast and M. Gomez, A discretization and multigrid solver for a Darcy–Stokes system of three dimensional vuggy porous media. *Comput. Geosci.* **13** (2009) 331–348.
- [4] L. Badea, M. Dacciaciatì and A. Quarteroni, Numerical analysis of the Navier–Stokes/Darcy coupling. *Numer. Math.* **115** (2010) 195–227.
- [5] F. Bai, D. Han, X. He and X. Yang, Deformation and coalescence of ferrodroplets in rosenzweig model using the phase field and modified level set approaches under uniform magnetic fields. *Commun. Nonlinear Sci. Numer. Simul.* **85** (2020) 105213.
- [6] A. Baskaran, J.S. Lowengrub, C. Wang and S.M. Wise, Convergence analysis of a second order convex splitting scheme for the modified phase field crystal equation. *SIAM J. Numer. Anal.* **51** (2013) 2851–2873.
- [7] G. Beavers and D. Joseph, Boundary conditions at a naturally permeable wall. *J. Fluid Mech.* **30** (1967) 197–207.

- [8] A. Bonito, J.-L. Guermond and S. Lee, Modified pressure-correction projection methods: open boundary and variable time stepping, in *Numerical Mathematics and Advanced Applications-ENUMATH 2013*. Vol. 103. Springer (2015).
- [9] A. Bonito, J.-L. Guermond and S. Lee, Numerical simulations of bouncing jets. *Int. J. Numer. Meth. Fluids* **80** (2016) 53–75.
- [10] Y. Boubendir and S. Tlupova, Domain decomposition methods for solving Stokes–Darcy problems with boundary integrals. *SIAM J. Sci. Comput.* **35** (2013) B82–B106.
- [11] F. Boyer, Mathematical study of multi-phase flow under shear through order parameter formulation. *Asymptot. Anal.* **20** (1999) 175–212.
- [12] S.C. Brenner, A.E. Diegel and L.-Y. Sung, A robust solver for a mixed finite element method for the Cahn–Hilliard equation. *J. Sci. Comput.* **77** (2018) 1234–1249.
- [13] G. Brereton and D. Korotney, Coaxial and oblique coalescence of two rising bubbles, in *Dynamics of Bubbles and Vortices Near a Free Surface*, edited by G. Tryggvason I. Sahin. Vol. 119. ASME (1991).
- [14] M. Cai, M. Mu and J. Xu, Numerical solution to a mixed Navier–Stokes/Darcy model by the two-grid approach. *SIAM J. Numer. Anal.* **47** (2009) 3325–3338.
- [15] Y. Cai, H. Choi and S. Shen, Error estimates for time discretizations of Cahn–Hilliard and Allen–Cahn phase-field models for two-phase incompressible flows. *Numer. Math.* **137** (2017) 417–449.
- [16] Y. Cao and X. Wang, The Beavers–Joseph interface boundary condition is well approximated by the Beavers–Joseph–Saffman–Jones interface boundary condition. *SIAM J. Sci. Comput.* **82** (2022) 1020–1044.
- [17] Y. Cao, M. Gunzburger, F. Hua and X. Wang, Coupled Stokes–Darcy model with Beavers–Joseph interface boundary condition. *Comm. Math. Sci.* **8** (2010) 1–25.
- [18] Y. Cao, M. Gunzburger, X.-M. He and X. Wang, Robin–Robin domain decomposition methods for the steady Stokes–Darcy model with Beaver–Joseph interface condition. *Numer. Math.* **117** (2011) 601–629.
- [19] Y. Cao, M. Gunzburger, X.-M. He and X. Wang, Parallel, non-iterative, multi-physics domain decomposition methods for time-dependent Stokes–Darcy systems. *Math. Comput.* **83** (2014) 1617–1644.
- [20] A. Çesmelioglu and B. Rivière, Analysis of time-dependent Navier–Stokes flow coupled with Darcy flow. *J. Numer. Math.* **16** (2008) 249–280.
- [21] A. Çesmelioglu and B. Rivière, Existence of a weak solution for the fully coupled Navier–Stokes/Darcy-transport problem. *J. Differ. Equ.* **252** (2012) 4138–4175.
- [22] A. Çesmelioglu, V. Girault and B. Rivière, Time-dependent coupling of Navier–Stokes and Darcy flows. *ESAIM Math. Model. Numer. Anal.* **47** (2013) 539–554.
- [23] I. Chakraborty, G. Biswas and P.S. Ghoshdastidar, A coupled level-set and volume-of-fluid method for the buoyant rise of gas bubbles in liquids. *Int. J. Heat Mass Tran.* **58** (2013) 240–259.
- [24] C. Chen and X. Yang, Fully-discrete finite element numerical scheme with decoupling structure and energy stability for the Cahn–Hilliard phase-field model of two-phase incompressible flow system with variable density and viscosity. *ESAIM Math. Model. Numer. Anal.* **55** (2021) 2323–2347.
- [25] W. Chen, M. Gunzburger, F. Hua and X. Wang, A parallel Robin–Robin domain decomposition method for the Stokes–Darcy system. *SIAM. J. Numer. Anal.* **49** (2011) 1064–1084.
- [26] J. Chen, S. Sun and X. Wang, A numerical method for a model of two-phase flow in a coupled free flow and porous media system. *J. Comput. Phys.* **268** (2014) 1–16.
- [27] W. Chen, D. Han and X. Wang, Uniquely solvable and energy stable decoupled numerical schemes for the Cahn–Hilliard–Stokes–Darcy system for two-phase flows in karstic geometry. *Numer. Math.* **137** (2017) 229–255.
- [28] P. Chidyagwai and B. Rivière, On the solution of the coupled Navier–Stokes and Darcy equations. *Comput. Methods Appl. Mech. Eng.* **198** (2009) 3806–3820.
- [29] V. DeCaria, W. Layton and M. McLaughlin, A conservative, second order, unconditionally stable artificial compression method. *Comput. Methods Appl. Mech. Eng.* **325** (2017) 733–747.
- [30] A.E. Diegel, X. Feng and S.M. Wise, Analysis of a mixed finite element method for a Cahn–Hilliard–Darcy–Stokes system. *SIAM J. Numer. Anal.* **53** (2015) 127–152.
- [31] M. Discacciati and L. Gerardo-Giorda, Optimized Schwarz methods for the Stokes–Darcy coupling. *IMA J. Numer. Anal.* **38** (2018) 1959–1983.
- [32] M. Discacciati and A. Quarteroni, Navier–Stokes/Darcy coupling: modeling, analysis, and numerical approximation. *Rev. Mat. Complut.* **22** (2009) 315–426.
- [33] M. Discacciati, P. Gervasio, A. Giacomini and A. Quarteroni, The interface control domain decomposition method for Stokes–Darcy coupling. *SIAM J. Numer. Anal.* **54** (2016) 1039–1068.
- [34] X. Feng, Y. He and C. Liu, Analysis of finite element approximations of a phase field model for two-phase fluids. *Math. Comp.* **76** (2007) 539–571.
- [35] X.L. Feng, T. Tang and J. Yang, Stabilized Crank–Nicolson/Adams–Bashforth schemes for phase field models. *East Asian J. Appl. Math.* **3** (2013) 59–80.
- [36] J.A. Fiordilino, W. Layton and Y. Rong, An efficient and modular grad-div stabilization. *Comput. Methods Appl. Mech. Eng.* **335** (2018) 327–346.
- [37] L. Formaggia, A. Quarteroni and A. Veneziani, *Cardiovascular Mathematics: Modeling and Simulation of the Circulatory System*. Springer-Verlag, New York (2009).
- [38] M. Gao and X. Wang, An efficient scheme for a phase field model for the moving contact line problem with variable density and viscosity. *J. Comput. Phys.* **272** (2014) 704–718.

- [39] Y. Gao, X. He, L. Mei and X. Yang, Decoupled, linear, and energy stable finite element method for the Cahn–Hilliard–Navier–Stokes–Darcy phase field model. *SIAM J. Sci. Comput.* **40** (2018) B110–B137.
- [40] Y. Gao, D. Han, X.-M. He and U. Rüde, Unconditionally stable numerical methods for Cahn–Hilliard–Navier–Stokes–Darcy system with different densities and viscosities. *J. Comput. Phys.* **454** (2022) 110968.
- [41] V. Girault and B. Rivière, DG approximation of coupled Navier–Stokes and Darcy equations by Beaver–Joseph–Saffman interface condition. *SIAM J. Numer. Anal.* **47** (2009) 2052–2089.
- [42] J.G. Gluyas and R.E. Swarbrick, *Petroleum Geology*. Blackwell Publishing (2004).
- [43] H. Gomez and T.J. Hughes, Provably unconditionally stable, second-order time-accurate, mixed variational methods for phase-field models. *J. Comput. Phys.* **230** (2016) 5310–5327.
- [44] Z. Guan, C. Wang and S.W. Wise, A convergent convex splitting scheme for the periodic nonlocal Cahn–Hilliard equation. *Numer. Math.* **128** (2014) 277–406.
- [45] J.-L. Guermond and L. Quartapelle, A projection FEM for variable density incompressible flows. *J. Comput. Phys.* **165** (2000) 167–188.
- [46] J.-L. Guermond, P. Mineev and J. Shen, An overview of projection methods for incompressible flows. *Comput. Methods Appl. Mech. Eng.* **195** (2006) 6011–6045.
- [47] F. Guillén-González and G. Tierra, On linear schemes for a Cahn–Hilliard diffuse interface model. *J. Comput. Phys.* **234** (2013) 140–171.
- [48] M. Gunzburger, X.-M. He and B. Li, On Ritz projection and multi-step backward differentiation schemes in decoupling the Stokes–Darcy model. *SIAM J. Numer. Anal.* **56** (2018) 397–427.
- [49] D. Han, D. Sun and X. Wang, Two-phase flows in karstic geometry. *Math. Methods Appl. Sci.* **37** (2014) 3048–3063.
- [50] D. Han, X. Wang and H. Wu, Existence and uniqueness of global weak solutions to a Cahn–Hilliard–Stokes–Darcy system for two-phase incompressible flows in karstic geometry. *J. Differ. Equ.* **257** (2014) 3887–3933.
- [51] X.-M. He, J. Li, Y. Lin and J. Ming, A domain decomposition method for the steady-state Navier–Stokes–Darcy model with Beavers–Joseph interface condition. *SIAM J. Sci. Comput.* **37** (2015) S264–S290.
- [52] M. Hintermüller, M. Hinze and C. Kahle, An adaptive finite element Moreau–Yosida-based solver for a coupled Cahn–Hilliard/Navier–Stokes system. *J. Comput. Phys.* **235** (2013) 810–827.
- [53] J. Hou, M. Qiu, X.-M. He, C. Guo, M. Wei and B. Bai, A dual-porosity-Stokes model and finite element method for coupling dual-porosity flow and free flow. *SIAM J. Sci. Comput.* **38** (2016) B710–B739.
- [54] G. Kanschat and B. Rivière, A strongly conservative finite element method for the coupling of Stokes and Darcy flow. *J. Comput. Phys.* **229** (2010) 5933–5943.
- [55] D. Kay and R. Welford, Efficient numerical solution of Cahn–Hilliard–Navier–Stokes fluids in 2D. *SIAM J. Sci. Comput.* **29** (2007) 2241–2257.
- [56] J. Kim, K. Kang, and J. Lowengrub, Conservative multigrid methods for Cahn–Hilliard fluids. *J. Comput. Phys.* **193** (2004) 511–543.
- [57] J. Kou, S. Sun and X. Wang, Linearly decoupled energy-stable numerical methods for multicomponent two-phase compressible flow. *SIAM J. Numer. Anal.* **56** (2018) 3219–3248.
- [58] J. Kou, X. Wang, S. Du and S. Sun, An energy stable linear numerical method for thermodynamically consistent modeling of two-phase incompressible flow in porous media. *J. Comput. Phys.* **451** (2022) 110854.
- [59] E. Kuniansky, Geological survey karst interest group proceedings, in U.S. Geological Survey Scientific Investigations Report 2008-5023. Bowling Green (2008). Open seminar.
- [60] W.J. Layton, F. Schieweck and I. Yotov, Coupling fluid flow with porous media flow. *SIAM J. Numer. Anal.* **40** (2002) 2195–2218.
- [61] S. Lee and A.J. Salgado, Stability analysis of pressure correction schemes for the Navier–Stokes equations with traction boundary conditions. *Comput. Methods Appl. Mech. Engrg.* **309** (2016) 307–324.
- [62] H.G. Lee, J. Lowengrub and J. Goodman, Modeling pinchoff and reconnection in a Hele–Shaw cell. I. The models and their calibration. *Phys. Fluids* **14** (2002) 492–513.
- [63] D. Li, Z.H. Qiao and T. Tang, Characterizing the stabilization size for semi-implicit Fourier-spectral method to phase field equations. *SIAM J. Numer. Anal.* **54** (2016) 1653–1681.
- [64] H.-L. Liao, T. Tang and T. Zhou, A second-order and nonuniform time-stepping maximum-principle preserving scheme for time-fractional Allen–Cahn equations. *J. Comput. Phys.* **414** (2020) 109473.
- [65] K. Lipnikov, D. Vassilev and I. Yotov, Discontinuous Galerkin and mimetic finite difference methods for coupled Stokes–Darcy flows on polygonal and polyhedral grids. *Numer. Math.* **126** (2014) 321–360.
- [66] C. Liu and J. Shen, A phase field model for the mixture of two incompressible fluids and its approximation by a Fourier-spectral method. *Phys. D* **179** (2003) 211–228.
- [67] J. Lowengrub and L. Truskinovsky, Quasi-incompressible Cahn–Hilliard fluids and topological transitions. *R. Soc. Lond. Proc. Ser. A Math. Phys. Eng. Sci.* **454** (1998) 2617–2654.
- [68] J. Matusick and P. Zanbergen, Comparative study of groundwater vulnerability in a karst aquifer in central florida. *Geophy. Res. Abst.* **9** (2007) 1–1.
- [69] M. Moraiti, On the quasistatic approximation in the Stokes–Darcy model of groundwater-surface water flows. *J. Math. Anal. Appl.* **394** (2012) 796–808.
- [70] M. Mu and J. Xu, A two-grid method of a mixed Stokes–Darcy model for coupling fluid flow with porous media flow. *SIAM J. Numer. Anal.* **45** (2007) 1801–1813.

- [71] M. Mu and X. Zhu, Decoupled schemes for a non-stationary mixed Stokes–Darcy model. *Math. Comp.* **79** (2010) 707–731.
- [72] Q. Pan, C. Chen, Y.J. Zhang and X. Yang, A novel hybrid IGA-EIEQ numerical method for the Allen–Cahn/Cahn–Hilliard equations on complex curved surfaces. *Comput. Methods Appl. Mech. Eng.* **404** (2023) 115767.
- [73] T. Qian, X. Wang and P. Sheng, Molecular scale contact line hydrodynamics of immiscible flows. *Phys. Rev. E* **68** (2003) 016306.
- [74] Z.H. Qiao, S. Sun, T. Zhang and Y. Zhang, A new multi-component diffuse interface model with Peng–Robinson equation of state and its scalar auxiliary variable (SAV) approach. *Commun. Comput. Phys.* **26** (2019) 1597–1616.
- [75] C. Qiu, X.-M. He, J. Li and Y. Lin, A domain decomposition method for the time-dependent Navier–Stokes–Darcy model with Beavers–Joseph interface condition and defective boundary condition. *J. Comput. Phys.* **411** (2020) #109400.
- [76] B. Rivière and I. Yotov, Locally conservative coupling of Stokes and Darcy flows. *SIAM J. Numer. Anal.* **42** (2005) 1959–1977.
- [77] H. Rui and Y. Sun, A MAC scheme for coupled Stokes–Darcy equations on non-uniform grids. *J. Sci. Comput.* **82** (2020) 79.
- [78] J. Shen and X. Yang, A phase-field model and its numerical approximation for two-phase incompressible flows with different densities and viscosities. *SIAM J. Sci. Comput.* **32** (2010) 1159–1179.
- [79] J. Shen and X. Yang, Numerical approximations of Allen–Cahn and Cahn–Hilliard equations. *Discrete Contin. Dyn. Syst.* **28** (2010) 1169–1691.
- [80] J. Shen and X. Yang, Decoupled, energy stable schemes for phase-field models of two-phase incompressible flows. *SIAM J. Numer. Anal.* **53** (2015) 279–296.
- [81] J. Shen, J. Xu and J. Yang, A new class of efficient and robust energy stable schemes for gradient flows. *SIAM Rev.* **61** (2019) 474–506.
- [82] S.K.F. Stoter, P. Müller, L. Cicalese, M. Tuveri, D. Schillinger and T.J.R. Hughes, A diffuse interface method for the Navier–Stokes/Darcy equations: perfusion profile for a patient-specific human liver based on MRI scans. *Comput. Methods Appl. Mech. Eng.* **321** (2017) 70–102.
- [83] C. Taylor and E. Greene, Quantitative approaches in characterizing karst aquifers, in U.S. Geological Survey Karst Interest Group Proceedings. Water Resources Investigations Report 01-4011 (2001).
- [84] K. Tuber, D. Pocza and C. Hebling, Visualization of water buildup in the cathode of a transparent PEM fuel cell. *J. Power Sources* **124** (2003) 403–414.
- [85] M. van Sint Annaland, N.G. Deen and J.A.M. Kuipers, Numerical simulation of gas bubbles behaviour using a three-dimensional volume of fluid method. *Chem. Eng. Sci.* **60** (2005) 2999–3011.
- [86] D. Vassilev and I. Yotov, Coupling Stokes–Darcy flow with transport. *SIAM J. Sci. Comput.* **31** (2009) 3661–3684.
- [87] X. Wang, L. Ju and Q. Du, Efficient and stable exponential time differencing Runge–Kutta methods for phase field elastic bending energy models. *J. Comput. Phys.* **316** (2016) 21–38.
- [88] Y. Wu, Y. Di, Z. Kang and P. Fakcharoenphol, A multiple-continuum model for simulating single-phase and multiphase flow in naturally fractured vuggy reservoirs. *J. Petrol. Sci. Eng.* **78** (2011) 13–22.
- [89] Y. Xia, Y. Xu and C.-W. Shu, Application of the local discontinuous galerkin method for the Allen–Cahn/Cahn–Hilliard system. *Commun. Comput. Phys.* **5** (2009) 821–835.
- [90] C. Xu and T. Tang, Stability analysis of large time-stepping methods for epitaxial growth models. *SIAM J. Numer. Anal.* **44** (2006) 1759–1779.
- [91] X. Yang, A novel fully decoupled scheme with second-order time accuracy and unconditional energy stability for the Navier–Stokes equations coupled with mass-conserved Allen–Cahn phase-field model of two-phase incompressible flow. *Int. J. Numer. Methods Eng.* **122** (2021) 1283–1306.
- [92] J. Yang and J. Kim, Energy dissipation-preserving time-dependent auxiliary variable method for the phase-field crystal and the Swift–Hohenberg models. *Numer. Algorithms* **89** (2022) 1865–1894.
- [93] X. Yang, J. Zhao and X.-M. He, Linear, second order and unconditionally energy stable schemes for the viscous Cahn–Hilliard equation with hyperbolic relaxation using the invariant energy quadratization method. *J. Comput. Appl. Math.* **343** (2018) 80–97.
- [94] J. Yang, S. Mao, X.-M. He, X. Yang and Y. He, A diffuse interface model and semi-implicit energy stable finite element method for two-phase magnetohydrodynamic flows. *Comput. Meth. Appl. Mech. Eng.* **356** (2019) 435–464.
- [95] P. Yue, J. Feng, C. Liu and J. Shen, A diffuse-interface method for simulating two-phase flows of complex fluids. *J. Fluid Mech.* **515** (2004) 293–317.
- [96] Y. Zhang, C. Zhou, C. Qu, M. Wei, X.-M. He and B. Bai, Fabrication and verification of a glass-silicon-glass micro-nanofluidic model for investigating multi-phase flow in unconventional dual-porosity porous media. *Lab Chip* **19** (2019) 4071–4082.
- [97] H. Zhang, X. Yang and J. Zhang, Stabilized invariant energy quadratization (S-IEQ) method for the molecular beam epitaxial model without slope section. *Int. J. Numer. Anal. Model.* **18** (2021) 642–655.
- [98] J. Zhao, X. Yang, J. Shen and Q. Wang, A decoupled energy stable scheme for a hydrodynamic phase-field model of mixtures of nematic liquid crystals and viscous fluids. *J. Comput. Phys.* **305** (2016) 539–556.
- [99] G. Zhu, J. Kou, J. Yao, A. Li and S. Sun, A phase-field moving contact line model with soluble surfactants. *J. Comput. Phys.* **405** (2020) 109170.

**Please help to maintain this journal in open access!**

This journal is currently published in open access under the Subscribe to Open model (S2O). We are thankful to our subscribers and supporters for making it possible to publish this journal in open access in the current year, free of charge for authors and readers.

Check with your library that it subscribes to the journal, or consider making a personal donation to the S2O programme by contacting [subscribers@edpsciences.org](mailto:subscribers@edpsciences.org).

More information, including a list of supporters and financial transparency reports, is available at <https://edpsciences.org/en/subscribe-to-open-s2o>.